AD-783 842

Nd-DOPED MIXED CRYSTAL LASER MATERIAL RESEARCH

W. C. Holton, et al

Texas Instruments, Incorporated

Prepared for:

Air Force Materials Laboratory
Advanced Research Projects Agency

July 1974

UNCLASSIFIED
SECURITY CLASSIFICATION OF THIS PAGE (When Data Entered)

REPORT DOCUMENTATION PAGE

READ INSTRUCTIONS
BEFORE COMPLETING FORM

1. REPORT NUMBER
AFML-TR-74-126

2. GOVT ACCESSION NO.

3. RECIPIENT'S CATALOG NUMBER
AD 783 842

4. TITLE (and Subtitle)
Nd-Doped Mixed Crystal Laser Material Research

5. TYPE OF REPORT & PERIOD COVERED
Final Report
1 July 1972 to 31 March 1974

6. PERFORMING ORG. REPORT NUMBER

7. AUTHOR(s)
W. C. Holton
D. W. Bellavance
F. J. Bruni
M. deWit
R. K. Watts

8. CONTRACT OR GRANT NUMBER(s)
F33615-72-C-1977

9. PERFORMING ORGANIZATION NAME AND ADDRESS
Texas Instruments Incorporated
Central Research Laboratories
Dallas, Texas 75222

10. PROGRAM ELEMENT, PROJECT, TASK AREA & WORK UNIT NUMBERS
Program Element: 61101E
Project: ARPA Order 2072
Job Order: 20720001

11. CONTROLLING OFFICE NAME AND ADDRESS
Advanced Research Projects Agency
1400 Wilson Boulevard
Arlington, Va. 22209

12. REPORT DATE
July 1974

13. NUMBER OF PAGES
106

14. MONITORING AGENCY NAME & ADDRESS (if different from Controlling Office)
Air Force Materials Laboratory
Air Force Systems Command
Wright-Patterson Air Force Base, Ohio 45433

15. SECURITY CLASS. (of this report)
Unclassified

15a. DECLASSIFICATION/DOWNGRADING SCHEDULE
N/A

16. DISTRIBUTION STATEMENT (of this Report)

Approved for public release; distribution unlimited

17. DISTRIBUTION STATEMENT (of the abstract entered in Block 20, if different from Report)

18. SUPPLEMENTARY NOTES

19. KEY WORDS (Continue on reverse side if necessary and identify by block number)

Mixed garnets
Laser material
Nd-doped
Yttrium aluminum garnet
Yttrium gallium garnet
High energy storage

20. ABSTRACT (Continue on reverse side if necessary and identify by block number)

The mixed crystal system $Y_3(Al_xGa_{1-x})_5O_{12}$ was investigated as a laser host material for Nd^{3+}. Spectroscopic studies established that at the optimum composition a reduction by a factor of 3 in gain, as compared with YAlG ($Y_3Al_5O_{12}$), is possible, implying increased output energy in Q-switched operation. Mechanical and thermal properties were found to be similar to those of YAlG.

DD FORM 1 JAN 73 1473 EDITION OF 1 NOV 65 IS OBSOLETE

UNCLASSIFIED
SECURITY CLASSIFICATION OF THIS PAGE (When Data Entered)

20. Abstract (continued)

Laser rods were fabricated from boules of the material, examined for optical quality, and tested under Q-switched conditions. The poor optical quality of the material, due largely to iridium inclusions and strain, precluded quantitative measurement of intrinsic laser parameters and a definitive comparison with YAℓG. Six laser rods were delivered under the contract.

It is concluded that although the mixed crystal material has potential advantages, it is not possible to realize this potential because of the difficulty of growing crystals of high optical quality. The difficulty is due to the volatility of gallia at the high growth temperatures and the sensitivity of composition to temperature fluctuations. While these problems might eventually be ameliorated somewhat in a research program of longer duration, it is possible that they could be circumvented entirely by choice of another mixed crystal system.

TABLE OF CONTENTS

SECTION PAGE

I INTRODUCTION 1
II OPTICAL SPECTROSCOPY 10
III ELECTRON PARAMAGNETIC RESONANCE 19
IV CRYSTAL GROWTH AND CHARACTERIZATION 26
- A. Phase Diagram 26
  - 1. Distribution Coefficients 28
  - 2. Lattice Parameter 28
- B. Material Sources 28
- C. Material Purity 29
- D. Material Preparation 29
- E. Crucibles 29
- F. Insulation 30
- G. Atmosphere 30
- H. Crystal Pullers 33
- I. Growth Parameters 33
  - 1. Atmosphere 34
  - 2. Pull Rate 35
  - 3. Rotation Rate 36
- J. Control 36
  - 1. Power Control 37
  - 2. Optical Diameter Control 38
- K. Results 38
  - 1. EPR Samples 38
  - 2. Spectroscopic Samples 39
  - 3. Laser Crystals 39
  - 4. Defects 39
- L. Discussion 51
  - 1. Atmosphere 54
  - 2. Pulling Rate 54

TABLE OF CONTENTS
(Continued)

SECTION PAGE

3. Rotation Rate 55
4. Control 55

M. Conclusions and Summary. 59

V PHYSICAL PROPERTIES MEASUREMENTS. 61

VI LASER TESTING 69

A. Introduction 69

B. Simple Theory. 72

C. Pump Cavity and Instrumentation. 74

D. Resonators and Q-Switches. 75

E. YAℓG:Nd Operation. 77

F. Twyman-Green Interferograms. 80

G. Nd Concentration 80

H. Long-Pulse Measurements. 83

I. Q-Switched Measurements. 83

J. Conclusions. 91

VII SUMMARY AND CONCLUSIONS 96

LIST OF ILLUSTRATIONS

FIGURE PAGE

1 Fluorescence Spectra and Energy Level Diagram for the $^4F_{3/2}$-$^4I_{11/2}$ Transitions in YAℓG:Nd^{3+} and YGaG:Nd^{3+} 3

2 Schematic Illustration of Inhomogeneous Broadening Mechanism in YAℓ_xGa$_{1-x}$G:Nd. 4

3 Measured Energy Levels of the $^4F_{3/2}$, $^4I_{11/2}$, and $^4I_{9/2}$ Multiplets for Nd in Al and Ga Garnets 11

4 Room-Temperature Emission Spectrum Near 1.06 μm for $Y_3A\ell_5O_{12}$, $Y_3(A\ell_{0.61}Ga_{0.39})O_{12}$, and $Y_3Ga_5O_{12}$ 12

5 Part of the Garnet Lattice in the Neighborhood of Yttrium Site (Cross-Hatched Ball) 20

LIST OF ILLUSTRATIONS

(Continued)

FIGURE PAGE

6 Resonance Field vs Angle for the Nd^{3+} Resonance in $Y_3A\ell_5O_{12}$ as the Magnetic Field is Rotated in the (110) Plane. 22

7 Low Field Resonance with the Field Along [001] (Marked g_z in Figure 11) for $Y_3A\ell_5O_{12}$ and Three Mixed Crystals 24

8 YAℓG-YGaG Phase Equilibria, Lattice Parameter 27

9 Furnace Design. 31

10 Seed Holder 32

11 YAGG #24. 40

12 YAGG #23. 41

13(a) Bubbles in Top Section of YAGG-50 (32X) 43

13(b) Bubbles and Precipitates Under the Surface of YAGG-50 (32X) 43

14 Striae in Crystal YAGG-40 Photographed Through Crossed Polarizers. 46

15(a) Section Through YAGG-46 47

15(b) Detail of a Heavy Stria 47

16 Striae in YAGG-34 48

17 Stria Spacings in YAGG-40 49

18 Stria Spacings in YAGG-34 50

19 Two Views of YAGG-49 Through Crossed Polarizers 52

20 Views of YAGG-49, Transmitted Light 53

21 The Effect of Seed Rotation Rate on Interface Shape 56

22(a) YAGG-59, As-Grown 57

22(b) Viewed Through Crossed Polarizers 57

22(c) Bottom Section of YAGG-59 57

23 YAGG No. 19 Showing Diameter Variations 58

24 Thermal Conductivity of Gallium Substituted YAG Crystals as a Function of Gallium Content. 62

25 Thermal Expansion of YAGG 65

26(a) Acousto-Optic Q-Switch and Resonator. 76

26(b) Electro-Optic Q-Switch and Resonator. 76

LIST OF ILLUSTRATIONS

(Continued)

FIGURE PAGE

27 Long Pulse and Q-Switched Performance of YAℓG:Nd in Experimental Resonator 78

28 High Input Energy Q-Switched Performance of YAG 79

29 Interferograms of the Six Mixed Crystal Laser Rods. 81

30 #23-1 Viewed through Crossed Polaroids. 82

31 Input-Output Curves Under Long Pulse Conditions 84

32 Known Mirror Losses vs the Observed Threshold Energies. 85

33 Calculated Values (Solid Lines) of $\sigma_s/2\pi$ vs R for Various Values of Loss L. 86

34 Input-Output Curves of YAG and YAGG:Nd. 87

35 Long-Pulse Operation of 45-B Before Rod Damage Occurred 89

36 Saturation in Rod 23-3. 90

37 Rod 47-A Q-Switched Operation 92

38 Rod 45-C Q-Switched Operation 93

39 Near Field Burn Patterns at 170 mJ for Rod 45-C 94

LIST OF TABLES

TABLE PAGE

I Laser Cross Sections for Nd Hosts 6

II Measured Peak Cross Sections (in Units of 10^{-19} cm^2) and Branching Ratios. 17

III Thermal Conductivities (W/cm K) 63

IV Thermal Conductivities Measured by Colora Thermoconductometer 64

V Thermal Expansion of YAGG 66

VI Refractive Index. 68

SECTION I

INTRODUCTION

The application of a pulsed Nd laser for surveillance and ranging, target illumination and designation, and weapons guidance generally requires a system with the following characteristics:

- High output power in Q-switched mode of operation
- High energy per pulse
- Fast repetition rate
- High average power
- High efficiency.

In addition, the laser should have physical characteristics consistent with the requirements for deployment in a military ordnance system. All known laser host materials have shortcomings with respect to one or more of these specifications.

The two most commonly used solid hosts for Nd are glass and YAℓG. Glass, because of its poor thermal conductivity, is severely limited in average power and pulse repetition rate. Furthermore, the efficiency that can be achieved is not competitive with that of YAℓG.

The limitation on YAℓG:Nd for pulsed laser systems application is its relatively high gain, resulting in saturation of the energy attainable in a Q-switched pulse due to the occurrence of amplified spontaneous emission at pump levels high above threshold. For the 1/4 inch x 3 inch laser rod typical of a YAℓG:Nd Q-switched oscillator system, energies of 200 to 250 millijoules are typical of the upper limit that is observed. An energy capability of 1 joule per pulse (at repetition rates of at least 10 pulses/sec) is a desirable goal in terms of the requirements of future military systems.

A number of approaches have been considered as solutions to this problem. An obvious possibility is the development of a laser material other than YAℓG:Nd which has a lower laser transition cross section. This parameter is determined by the odd crystal field, which mixes in opposite-parity configurations to the $4f^n$ configurations, permitting parity-forbidden electric-dipole transitions to occur within the $4f^n$ configuration. Thus, the absorption strengths of the pump bands, and therefore the efficiency, will generally be reduced along with the laser transition cross section in these lower gain materials. Furthermore, unless the excellent physical characteristics of YAℓG are maintained in the new material, it will not maintain its competitiveness, in spite of the increased Q-switch energy.

To answer this need, Texas Instruments has developed the concept of mixed crystal laser materials, particularly $YA\ell_xGa_{1-x}G$:Nd. Since YAℓG and YGaG are isostructural, it is possible to grow $YA\ell_xGa_{1-x}G$ with $0 \le x \le 1$. The crystal fields for the two compounds are sufficiently different, however, to yield a substantial difference in the Nd spectra. This situation is in contrast to the case of rare earth substitution for Y^{3+} ions, where the crystal field does not change substantially. There is only a slight difference, for example, between the crystal fields of YAℓG and LuAℓG.

The $^4F_{3/2}$ to $^4I_{11/2}$ transitions of Nd are shown in Figure 1 for both YAℓG and YGaG. The mixed crystal will have a distribution of Nd sites ranging from sites surrounded by all Aℓ ions to all Ga ions on the 10 nearest-neighbor sites. Therefore, the crystal field varies from site to site, and there is a range of wavelengths for the resulting spectral line. For a random distribution of Ga ions on Aℓ sites, this line will be a weighted Gaussian superposition of the Lorentzian components at each crystal field. Other distributions of Ga ions would result in somewhat different lineshapes; for example, a distribution in which the Aℓ and the Ga ions tend to cluster separately would result in a more rectangular lineshape. These possible behaviors are illustrated schematically in Figure 2.

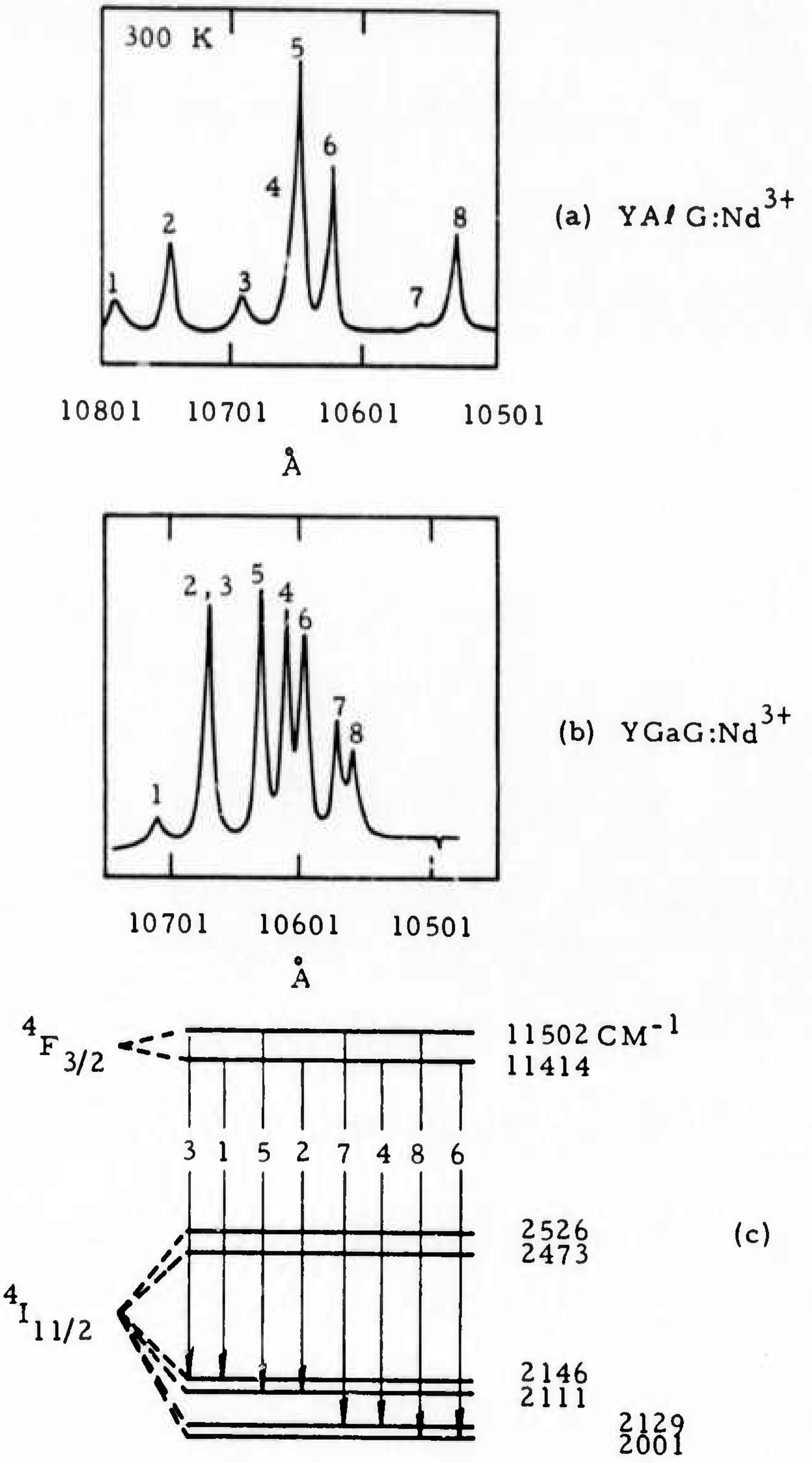

Figure 1 Fluorescence Spectra and Energy Level Diagram for the $^4F_{3/2}$-$^4I_{11/2}$ Transitions in YAℓG:Nd^{3+} and YGaG:Nd^{3+}. (a) Fluorescence spectra of Nd^{3+} $^4F_{3/2}$ → $^4I_{11/2}$ transitions in YAℓG; (b) Fluorescence spectra of Nd^{3+} $^4F_{3/2}$ → $^4I_{11/2}$ transitions in YGaG; (c) Nd^{3+} $^4F_{3/2}$ and $^4I_{11/2}$ energy levels showing the numbering of the transitions. The level positions are those for YAℓG.

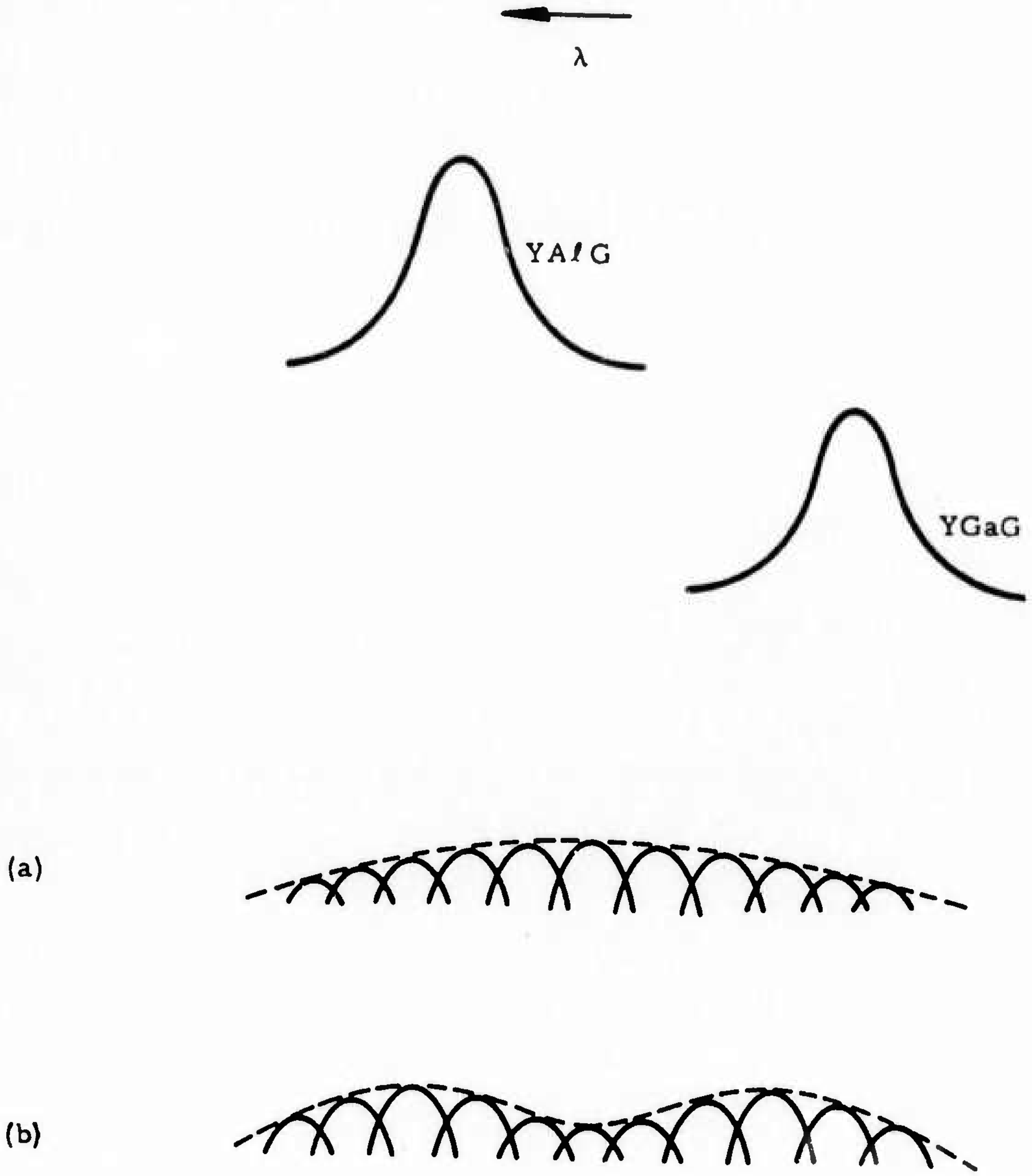

Figure 2 Schematic Illustration of Inhomogeneous Broadening Mechanism in $YA\ell_xGa_{1-x}G$:Nd. (a) Broadening for random distribution of crystal fields, (b) broadening for probability distribution peaking at Aℓ-rich and Ga-rich sites.

The integrated area under the spectral line is constant, since the radiative rate is a higher order effect of the crystal field (i.e., the mixing of opposite-parity configurations via the odd crystal field) and will not be changed substantially. Therefore, the gain is reduced by approximately the factor by which the line is broadened. This is strictly true only if the lineshape is the same. The gain reduction is even greater for the cases discussed above, particularly for the rectangle-like lineshape in the clustered ion case.

It is this phenomenon which results in the broad spectrum of Nd (and other rare-earth ions) in glass. The distribution in an amorphous solid might be expected to be far wider than it is, but it has been recently demonstrated by Mann and DeShazer[1] through a detailed analysis of the composite lineshape in Nd:glass that the basic environment is a Nd_2O_3 complex, and the distribution is in the outer environment surrounding the Nd_2O_3 group. Therefore, linewidths of Nd^{3+} laser transitions in glasses are only of the order of 100 cm^{-1}.

Returning to the case of the mixed crystal $YA\ell_xGa_{1-x}G$, the result is a theoretical reduction in the gain of the laser transition by as much as a factor of six and, consequently, a sixfold increase in the energy storage. Furthermore, this improvement in energy per pulse is achieved while maintaining the other attractive properties of YAℓG, specifically, the efficiency.

In particular, for 10% Ga doping, theory predicts a factor of 1.5 lower gain; for 50% Ga doping we would expect to obtain a factor of six lower gain. The anticipated laser cross sections (gain) for various Ga dopings are listed in Table I, with those for YAℓG,[2] glass,[3] and $YA\ell O_3$[4] included for comparision. The energy storage of $YA\ell O_3$ over YAℓG is only a factor of two (rather than the 2.5 factor of difference in the cross sections) because the amplified spontaneous emission probably does not occur in the (axial) low-gain direction.

Table I

Laser Cross Sections for Nd Hosts

Material	Cross Section
YAlG	6×10^{-19} cm^2
Glass	0.3×10^{-19} cm^2
$YAlO_3$ (low-gain direction)	2.5×10^{-19}
$YAl_{0.9}Ga_{0.1}G$	4×10^{-19} cm^2
$YAl_{0.7}Ga_{0.3}G$	2×10^{-19} cm^2
$YAl_{0.5}Ga_{0.5}G$	1×10^{-19} cm^2

Taking the conservative estimate of a maximum energy per pulse of 200 to 250 mJ for a conventional YAℓG:Nd laser rod 1/4 inch x 3 inch, theory projects an achievement of at least 1 Joule per pulse with $YA\ell_xGa_{1-x}G$ for a rod of the same size. This is approximately the range of pulse energy required by future system applications.

The mixed crystal material theoretically has an efficiency competitive with that of conventional YAℓG:Nd. The broadening of the laser transition will not affect the efficiency in pulsed operation, and the factor of two change in the branching ratio will affect the efficiency only slightly. The weak component of the 1.0641 line in YAℓG, which is shifted 40 cm^{-1} in $YA\ell_{0.5}Ga_{0.5}G$ and which takes up most of the factor of two change in intensity (see Figure 1), still contributes to the laser output in the mixed material in pulsed operation.

Furthermore, there is an additional contribution to the efficiency due to the broadening of the pump bands resulting from the same mechanism. Absorption spectra measurements of both YAℓG:Nd and YGaG:Nd have shown the broadening in mixed crystals is, on the average, of the same magnitude as in the laser transition. Since the absorptions are nearly optically thick, the broadening results in increased overlap with the pump source without a proportional loss in absorption strength. This can be demonstrated in a simple way. For 1.5% Nd in YAℓG, the average absorption coefficient is about 5 cm^{-1}. The resultant fractional power absorbed at the peak of the line in a 1/4 inch rod through a diameter is given by

$$P_{abs} = \frac{I_0 - I}{I_0} = 1 - e^{(0.6)(5)} \cong 95\%. \qquad (1)$$

A broadening of the line by a factor of three will result in a decrease in the absorption coefficient by a factor of three. The power absorbed now is

$$P_{abs} = \frac{I_0 - I}{I_0} = 1 - e^{(0.6)(1.7)} \cong 65\%. \qquad (2)$$

But the line is now three times broader, so the total integrated power absorbed relative to YAℓG is

$$\frac{(P_{abs})_{YA\ell_{0.5}Ga_{0.5}G}}{(P_{abs})_{YA\ell G}} = \frac{3(0.65)}{0.95} \cong 2 \ . \qquad (3)$$

Thus, there is twice as much absorption as in YAℓG. This has the effect of compensating for the decreased branching ratio and may even result in <u>increasing</u> the efficiency relative to YAℓG.

An additional projected feature of the mixed garnet was the probability that increased amounts of Nd may be incorporated without the accompanying optical degradation and concentration quenching to the extent that is observed in YAℓG:Nd. The decrease in optical degradation would result from the increased distribution coefficient for Nd in the mixed crystal, due to the increased unit cell size. The decrease in concentration quenching would result from the increased inhomogeneous broadening and the corresponding decrease in spectral overlap for ions in different sites. This will be true if resonant energy transfer is involved in the observed concentration quenching. That this may be true is indicated by the fact that other Nd laser materials for which inhomogeneous broadening is dominant, such as glass, show a retarded onset of concentration quenching as the neodymium concentration is raised. In conclusion, theory projects efficiencies for the new material in pulsed operation of at least 1 to 2% overall, which is the same as that observed in conventional YAℓG.

Spectroscopic examination of material grown in this program has confirmed these expectations, as described in Section II.

Since YAℓG and YGaG are both isostructural and congruently melting, it is possible to grow mixed crystals of $YA\ell_xGa_{1-x}G$, where $0 \leq x \leq 1$. On the other hand, since the ionic radius of $A\ell^{3+}$ is 0.51 Å, while that of Ga^{3+} is 0.62, one would expect serious problems in growing large, laser-quality mixed crystals. Furthermore, a significant vapor pressure difficulty had been reported for YGaG, resulting in Ga loss from the melt, a problem to be anticipated for the mixed crystals system as well. These anticipated difficulties have been borne out by the experiments detailed in Section IV.

SECTION II

OPTICAL SPECTROSCOPY

The main goal of the optical spectroscopic study was to determine the mixed crystal composition at which maximum cross section reduction of the most intense line occurs, and to measure the cross section at this optimum composition.

Figure 3 shows the relevant energy levels of Nd^{3+} in YAG and in YGG. The positions of these levels were determined by absorption and luminescence measurements at room temperature. They differ only slightly from the positions measured at low temperatures.[5] As can be seen from emission spectra shown in Figure 4, for both crystals the b → 3 transition is the strongest of the twelve $^4F_{3/2} \rightarrow {}^4I_{11/2}$ transitions. For YAG, this line is not resolved from the weaker a → 2 line; in YGG the two lines are well separated; in the mixed crystal, $Y_3(A\ell_{0.61}Ga_{0.39})_5O_{12}$, the lines are partially unresolved due to the inhomogeneous broadening. These emission spectra were observed using broad-band excitation, primarily into the $^4F_{3/2}$ to $^4G_{11/2}$ levels, with the crystal at room temperature. Since in our spectroscopic samples the Nd^{3+} concentration is less than 1%, the principal decay route is radiative decay from the $^4F_{3/2}$ level following nonradiative transitions to this level from higher-lying levels.

The peak cross section σ_m and the branching ratios are defined in the following manner: The populations of the two components a and b of $^4F_{3/2}$ are in thermal equilibrium, the rapid a ↔ b phonon-induced transitions determining the homogeneous contribution to the widths of the levels. The ratio of the level populations is then

$$N_b/N_a = \exp\left[-(E_b - E_a)/kT\right] = \eta \; . \qquad (4)$$

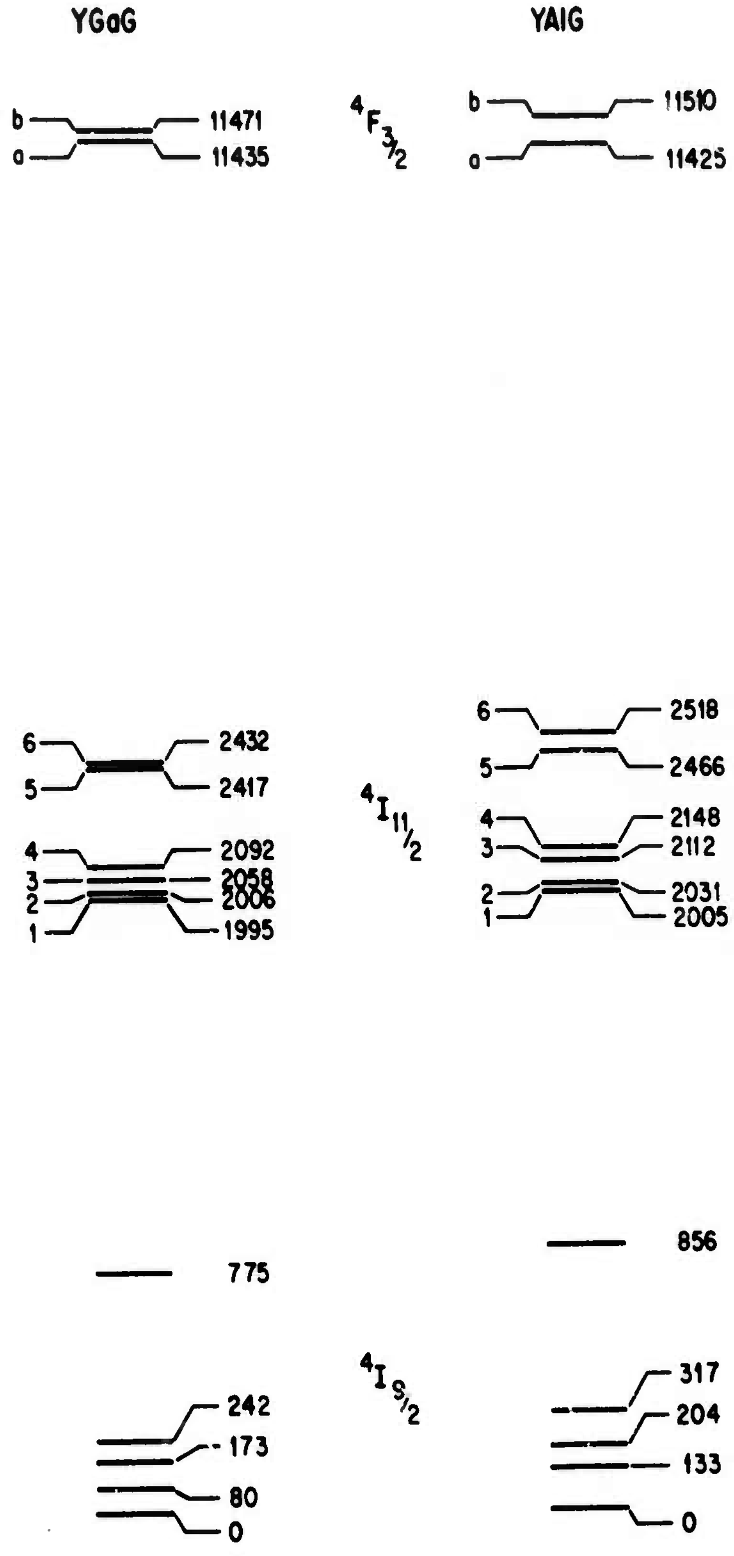

Figure 3 Measured Energy Levels of the $^4F_{3/2}$, $^4I_{11/2}$, and $^4I_{9/2}$ Multiplets for Nd in Al and Ga Garnets. Energy is in cm^{-1}.

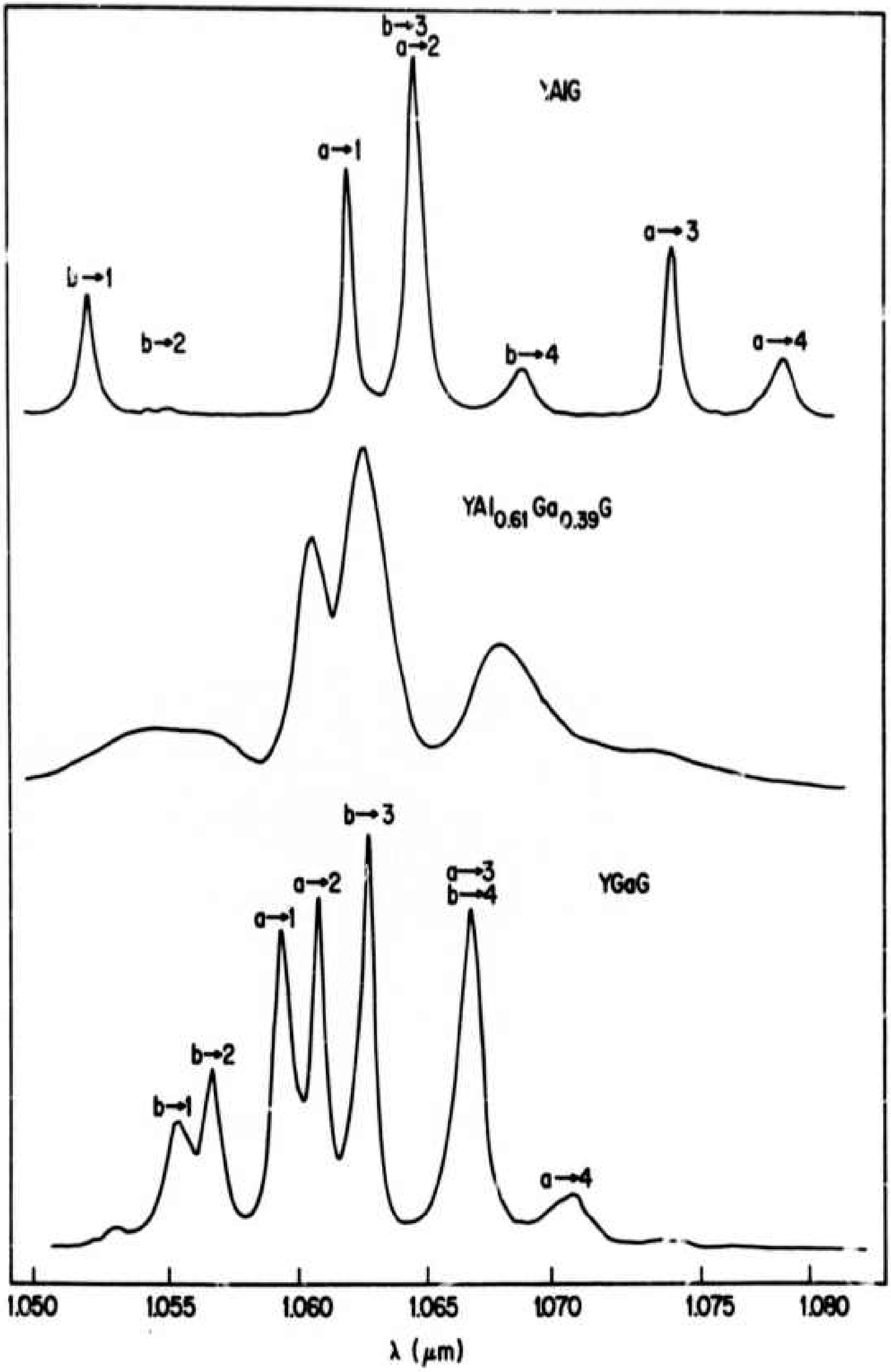

Figure 4 Room-Temperature Emission Spectrum Near 1.06 μm for $Y_3Al_5O_{12}$, $Y_3(Al_{0.61}Ga_{0.39})O_{12}$, and $Y_3Ga_5O_{12}$. The transitions are marked in accordance with the notation of Figure 3.

N_a and N_b decay radiatively with time constant τ. If A_{ij} is the spontaneous radiative emission rate per atom from level i to level j, then

$$\tau^{-1} = (1 + \eta)^{-1} \Sigma_j \, (A_{aj} + \eta A_{bj}). \qquad (5)$$

The sum is over all the crystal field components of the lower multiplets $^4I_{15/2}$, $^4I_{13/2}$, $^4I_{11/2}$, and $^4I_{9/2}$. The toal radiative decay rate of $^4F_{3/2}$ is

$$\frac{d}{dt} (N_a + N_b) = -N_a \Sigma_j \, (A_{aj} + \eta A_{bj}). \qquad (6)$$

The rate into the a → k transition is $-N_a A_{ak}$. The branching ratio β_{ak} is defined as the number of photons emitted per unit time in the a → k transition divided by the total number per unit time emitted from a and b, and is thus given by

$$\beta_{ak} = A_{ak} \, [\Sigma_j \, (A_{aj} + \eta A_{bj})]^{-1}. \qquad (7)$$

Similarly, β_{bk} may be expressed as

$$\beta_{bk} = \eta A_{bk} \, [\Sigma_j \, (A_{aj} + \eta A_{bj})]^{-1}. \qquad (8)$$

We assume with Kushida, et al.,[6] that the transitions are completely radiative. The spontaneous radiative emission rate is related to the emission cross section $\sigma_{ij}(\nu)$ by

$$A_{ij} = 8\pi n^2 \lambda_{if}^{-2} \int \sigma_{if}(\nu) d\nu. \qquad (9)$$

where λ_{ij} is the vacuum wavelength of the narrow emission line i → j, and n is the index of refraction of the crystal at the wavelength λ_{ij}. For Lorentzian or Gaussian line shapes the integral of σ is given in terms of the width of the line at half-maximum $\Delta\nu$ and the peak cross section σ_m by

$$\int \sigma_{ij}(\nu)\,d\nu = \tfrac{1}{2}\pi(\Delta\nu)_{ij}(\sigma_m)_{ij} \text{ (Lorentzian)},$$

or (10)

$$\tfrac{1}{2}(\pi/\ln 2)^{1/2}(\Delta\nu)_{ij}(\sigma_m)_{ij} \text{ (Gaussian)}.$$

For a line of arbitrary shape we shall define a lineshape parameter γ by the relation,

$$\int \sigma_{ij}(\nu)\,d\nu = \gamma_{ij}(\Delta\nu)_{ij}(\sigma_m)_{ij}. \tag{11}$$

Two methods were used to measure σ_m. In the first method $(\sigma_m)_{0j}$ is measured in an absorption experiment. 0 is the lowest member of the ground multiplet $^4I_{9/2}$ and j is either a or b. $(\sigma_m)_{0j} = N_0^{-1}(\alpha_m)_{0j}$, where N_0 is the number of ions in state 0 per cm^3, and α is the absorption coefficient. $\sigma_{0j} = \sigma_{j0}$ because the degeneracy of each level is 2. Then, by comparing the peak luminescence intensity of the j → 0 transition with that of the j → k transition of interest, one determines $(\sigma_m)_{jk}$. This method depends on an accurate measurement of the Nd concentration, from which N_0 is obtained. Because the concentration measurement was found to have rather large uncertainty, this method was less accurate than the second method described below, and all reported results were obtained by the second method. However, the results by the first method were in agreement with the second method.

The second method involves measurement of β and τ, which are related, according to Equations (5), (7), and (8) by

$$\beta_{aj} = (1 + \eta)^{-1}\tau A_{aj},$$

$$\beta_{bj} = \eta(1 + \eta)^{-1}\tau A_{bj}. \tag{12}$$

When β_{ij} and τ are known, A_{ij} can be obtained from Equation (9). From Equations (9) and (11), $(\sigma_m)_{ij}$ can then be calculated. At room temperature in $Y_3A\ell_5O_{12}$ and in many of the mixed crystals the a → 2 and b → 3 laser transitions are not resolved. In this case the sum

$$A_{b3} + \eta^{-1}A_{a2} = (1 + \eta)\eta^{-1}(\beta_{b3} + \beta_{a2}) \tag{13}$$

is obtained. The peak cross section of the composite line σ_m^* is measured, where

$$\gamma^*(\Delta\nu)^*\sigma_m^* = \gamma_{b3}(\Delta\nu)_{b3}(\sigma_m)_{b3} + \eta^{-1}\gamma_{a2}(\Delta\nu)_{a2}(\sigma_m)_{a2}.$$

γ^* and $(\Delta\nu)^*$ are measured from the composite line shape.

The β_{ij} were obtained from the luminescence spectrum measured with a spectrometer of calibrated response. A 0.75-m Spex monochromator with 1200 lines/mm grating and an InAs detector cooled to 77 K were used. The response was calibrated with a tungsten-halogen standard lamp. It was assumed that 62% of the quanta emitted from $^4F_{3/2}$ were emitted into the $^4F_{3/2} \rightarrow {}^4I_{11/2}$ (a,b → 1,2,3,4,5,6) transitions. For YAG, the $^4F_{3/2} \rightarrow {}^4I_{11/2}$ branching ratio was found by Kushida, Marcos, and Geusic[6] to be 0.60 ±10% and by Watts[7] to be 0.65 ±15%. This ratio should be insensitive to host crystal. The energy levels of Nd^{3+} in YAG and YGG are quite similar, as can be seen from Figure 3.

Thus the branching ratio $^4F_{3/2} \rightarrow {}^4I_{11/2}$ is assumed to be independent of x and taken to be 0.62 for all compositions $Y_3(A\ell_{1-x}Ga_x)_5O_{12}$. DeShazer and Komai[8] found this branching ratio to be 0.60 in barium crown glass, a very different host. Therefore, only the 12 lines $^4F_{3/2}a,b \rightarrow {}^4I_{11/2}1,2,3,4,5,6$ were measured.

The refractive index n was measured by the method of minimum deviation and found to be 1.815 for YAG, 1.824 for $YA\ell_{0.9}Ga_{0.1}G$, and 1.915 for YGG at 1.06 μm. For other compositions a linear interpolation was used. Table II displays the measured branching ratios and peak cross sections for the a → 2 and b → 3 transitions, or for the composite line when these are not resolved. For YAG, although the two lines are completely unresolved, since their shapes are Lorentzian, a decomposition of the composite line was possible with the aid of a computer. From Table II it can be seen that although β_{a2} and β_{a3} vary considerably from YAG to YGG, their sum is constant. $(\sigma_m)_{b3}$ decreases by a factor of 2 from YAG to YGG, but $(\sigma_m)_{a2}$ remains nearly constant. The a → 2 and b → 3 lines are nearly completely resolved for YGG, and $(\sigma_m)_{b3} \approx \sigma_m^*$. For $Y_3(A\ell_{1-x}Ga_x)_5O_{12}$ with $x = 0.94$ and $x = 0.86$, these transitions are rather well resolved; only the cross section of the most intense line was measured in these cases. For the compositions near the middle of the range, $x \approx 0.5$, it is not obvious which value of η to use. The factor $\eta^{-1}(1 + \eta)$ varies from 2.2 for YAG to 2.5 for YGG, a small range of variation. For $x < 0.5$, the value for YAG was used, and for $x > 0.5$, the value for YGG. The tabulated values of σ_m^* are considered accurate to within ± 15% for $x = 0$ and $x = 1$ and ±20 - 25% for other compositions. The measured value for YAG, $\sigma_m^* = 9.8 \times 10^{-19}$ cm^2 can be compared with 8.8×10^{-19} cm^2 ±10%, measured by Kushida, Marcos, and Geusic.[6] These are the same within experimental accuracy. Nd concentration of the samples was in the range 0.1 - 0.5 at .%.

At the optimum concentration, a reduction in σ_m^* by a factor of 3.3 compared with YAG is observed. A larger reduction would have been observed had the a → 2,

Table II

Measured Peak Cross Sections (in Units of 10^{-19} cm^2) and Branching Ratios

Crystal		β_{b3}	β_{a2}	$(\sigma_m)_{b3}$	$(\sigma_m)_{a2}$	$\beta_{b3}+\beta_{a2}$	σ_m^*	τ(μ sec)
Commercial	YAlG	0.135	0.045	7.0	1.9	0.18	9.8	232
23	$YAl_{0.88}Ga_{0.12}G$					0.18	4.8	247
19	$YAl_{0.78}Ga_{0.22}G$					0.18	4.2	245
5	$YAl_{0.61}Ga_{0.39}G$					0.17	3.3	246
S-14	$YAl_{0.45}Ga_{0.55}$					0.17	3.4	278
S-13	$YAl_{0.31}Ga_{0.69}G$					0.20	3.0	269
S-12	$YAl_{0.14}Ga_{0.86}G$						3.4	257
S-11	$YAl_{0.06}Ga_{0.94}G$						3.8	257
S-10	YGaG	0.10	0.066	3.3	2.1	0.17	3.7	270

b → 3 separation increased more rapidly with increasing x. As x increases from zero to unity, the inhomogeneous component of the linewidth initially increases, reaches a maximum, and then decreases. The a → 2, b → 3 separation increases monotonically with increasing x. At the composition of maximum broadening, the overlap of the a → 2 and b → 3 lines is still so great that the most intense peak has a σ_m^* substantially enhanced by this overlap.

It was found that by exciting the $^4F_{3/2} \rightarrow {}^4I_{11/2}$ luminescence with a tunable dye laser at 2K different types of Nd^{3+} ions could be selectively excited. (A type is characterized by a particular Ga/Aℓ near environment.) As the temperature is raised, spectral diffusion of excitation across the composite line becomes faster. At room temperature this process is much faster than the decay of $^4F_{3/2}$ so that the line behaves like a homogeneously broadened line. It is not known how the speed of spectral diffusion compares with the time required for the development of Q-switched output (∼ 100 nsec).

SECTION III

ELECTRON PARAMAGNETIC RESONANCE

In order to investigate the microscopic nature of the Nd-Ga association, which leads to the inhomogeneous broadening of the optical spectra, electron paramagentic resonance of the Nd^{3+} was studied.

Although the garnet lattice has an overall cubic structure with space group O_h^{10}, the symmetry at the site of yttrium, for which rare earths substitute, is orthorhombic. The low-symmetry crystal field removes all degeneracy except Kramers degeneracy of an ion with an odd number of electrons, splitting each multiplet $^{2S+1}L_J$ into $J + \frac{1}{2}$ Kramers doublets. Nine independent parameters are necessary to describe this crystal field. The crystal field splitting of Nd^{3+} in $Y_3Al_5O_{12}$ and $Y_3Ga_5O_{12}$ has been analyzed using five crystal field parameters under the assumption that the field is nearly tetragonal. Wavefunctions from which g factors could be calculated have not been published.

Figure 5 shows an yttrium site and the nearest surrounding atoms. Yttrium has as nearest neighbors eight oxygen atoms located at the corners of a distorted cube. The nearest aluminum atoms are of two types. Each aluminum of the first type is octahedrally coordinated by six oxygen atoms. There are four of this type with respect to which the yttrium is tetrahedrally coordinated. Each aluminum of the second type is tetrahedrally coordinated by four nearest oxygen atoms. There are six of this type, two of which lie along the [001] axis and are nearer the central yttrium than the other four. (The others do not lie along the [100] axes, where the origin is taken at the yttrium site.) Figure 5 shows one type of yttrium site. Another type is oriented in the same way with respect to [100], [010], and [00$\bar{1}$] as the one shown is oriented with respect to [100], [010], and [001]. There are also four other types oriented similarly along the other $\langle 100 \rangle$ directions.

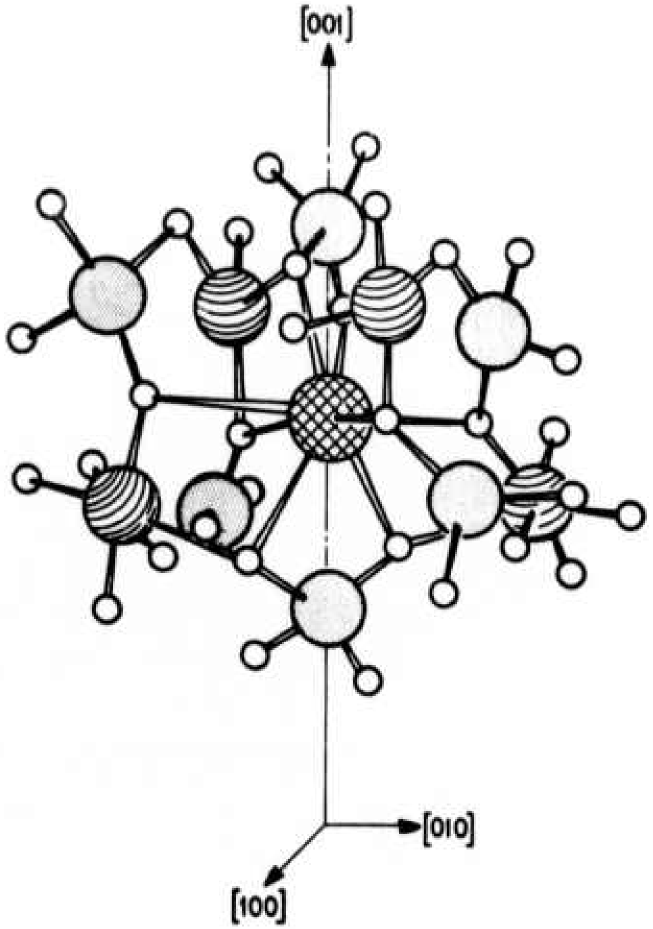

Figure 5 Part of the Garnet Lattice in the Neighborhood of Yttrium Site (Cross-Hatched Ball). The oxygens are shown as small open circles. The other balls are aluminums. Those coordinated by six oxygens are striped. Those coordinated by four oxygens are dotted; two of these lie along the [001] axis.

Electron paramagnetic resonance (EPR) spectra were taken at 1.3 K and 9.16 GHz on crystals containing Nd^{142} at a concentration of 10^{18} cm^{-3} (0.008 at. %). These are crystals I-1, I-2, ..., I-9. The isotope was used because the absence of hyperfine structure simplifies the spectra. The splitting of the ground doublet in a magnetic field is described for $Y_3Al_5O_{12}$ and $Y_3Ga_5O_{12}$ by the spin Hamiltonian:

$$\mathcal{H} = g_x\beta H_x S_x + g_y\beta H_y S_y + g_z\beta H_z S_z. \qquad (14)$$

The effective spin $S = \frac{1}{2}$. This spin Hamiltonian is written in the conventional[9] axis system x, y, z = $[1\bar{1}0]$ or $[110]$, $[110]$ or $[1\bar{1}0]$, $[001]$. There are, of course, five other magnetically inequivalent sites, as discussed above. There is also an ambiguity in the relation of the g tensor to the type of site producing the resonance. It is not possible to determine whether the g tensor z axis corresponds to the [001] axis of Figure 5. It could correspond instead to the [010] or to the [100] axis of the figure. This ambiguity might be resolved for example by an electron-nuclear double resonance (ENDOR) experiment.

Figure 6 shows the angular dependence of the resonance field versus orientation of the static field when the static field is rotated in the $(1\bar{1}0)$ plane. Resonances from the six types of center are shown. The g factors measured for $Y_3Al_5O_{12}$ are

$$g_x = 1.742, \; g_y = 1.160, \; g_z = 3.906.$$

These values are similar to those measured by Wolf, et al.[10] In addition to the resonances shown in Figure 6, other much weaker lines were present. They generally broadened rapidly as the field was rotated away from a principal direction, and were not investigated in detail.

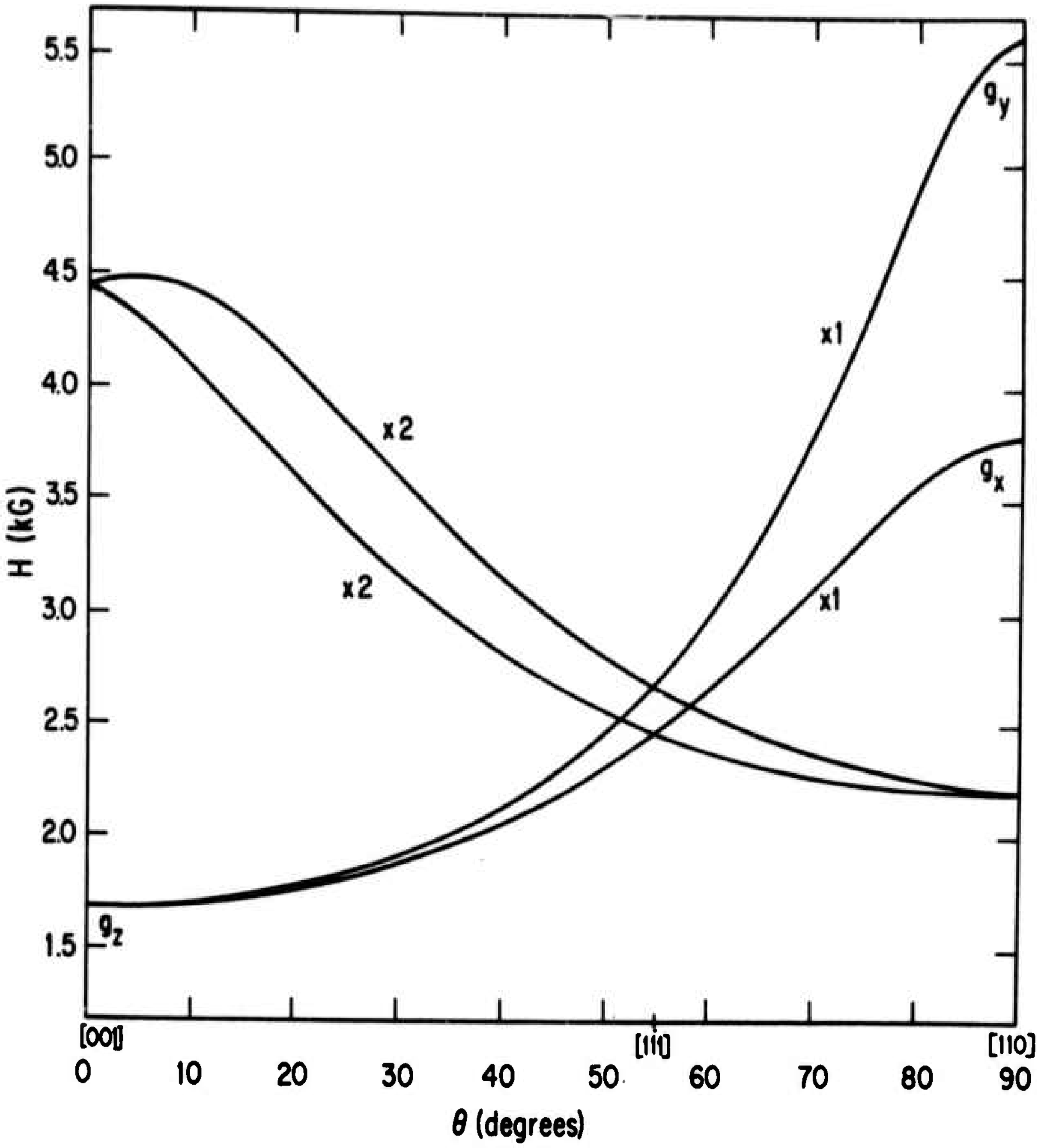

Figure 6 Resonance Field vs Angle for the Nd^{3+} Resonance in $Y_3Al_5O_{12}$ as the Magnetic Field is Rotated in the $(1\bar{1}0)$ Plane. θ is the angle between the field and [001]. Two of the curves represent resonance of twice as many centers as the other two and are labeled 2. Thus there are four curves rather than six. The resonance frequency is 9.16 GHz. The symbols g_x, g_y, and g_z indicate the extrema where these principal values are measured.

Spectra were also taken of mixed crystals with x = 0.008, 0.04, 0.083, 0.12, and 0.34. As x increases from zero, the lines just described become increasingly broad, some line shapes becoming asymmetric. In addition, many other weaker lines appear. When the field is rotated away from a principal direction, most of these broaden and become impossible to follow over a wide angular range. Two could be studied in detail and will be called satellite No. 1 and satellite No. 2. The resonance field of each satellite has turning points along the z and y axes, and therefore both have the same g tensor axes as those of the main resonance. For x = 0.008, the g factors are

$$g_y(1) = 1.100, \qquad g_y(2) = 1.201,$$

$$g_z(1) = 3.869, \qquad g_z(2) = 3.907.$$

g_x was not measured for these satellites. Satellite No. 1 is shown in Figure 7 for H along the z axis, the position where all lines are narrowest. Satellite No. 2 is not resolved from the main line at this orientation. For x = 0.34, satellite No. 1 also cannot be resolved from the main line at this orientation.

Let us assume that these satellites are due to Nd ions with one or more of the ten nearest Aℓ's replaced by Ga, and that substitution of Ga at more distant Aℓ sites leads only to line broadening. The resonance from a Nd with a Ga substitutional along one of the g tensor axes mentioned above will be characterized by a g tensor with the same principal axes but different principal values. If the substitution occurs at a site not located along one of these axes, the resonance will, in general, be described by a g tensor with axes rotated with respect to those of Nd in $Y_3A\ell_5O_{12}$. From Figure 5, only the two nearest aluminum sites are on a g tensor axis - the z axis. We therefore assume that the two satellites are due to Nd ions with one and two Ga's replacing these two Aℓ's.

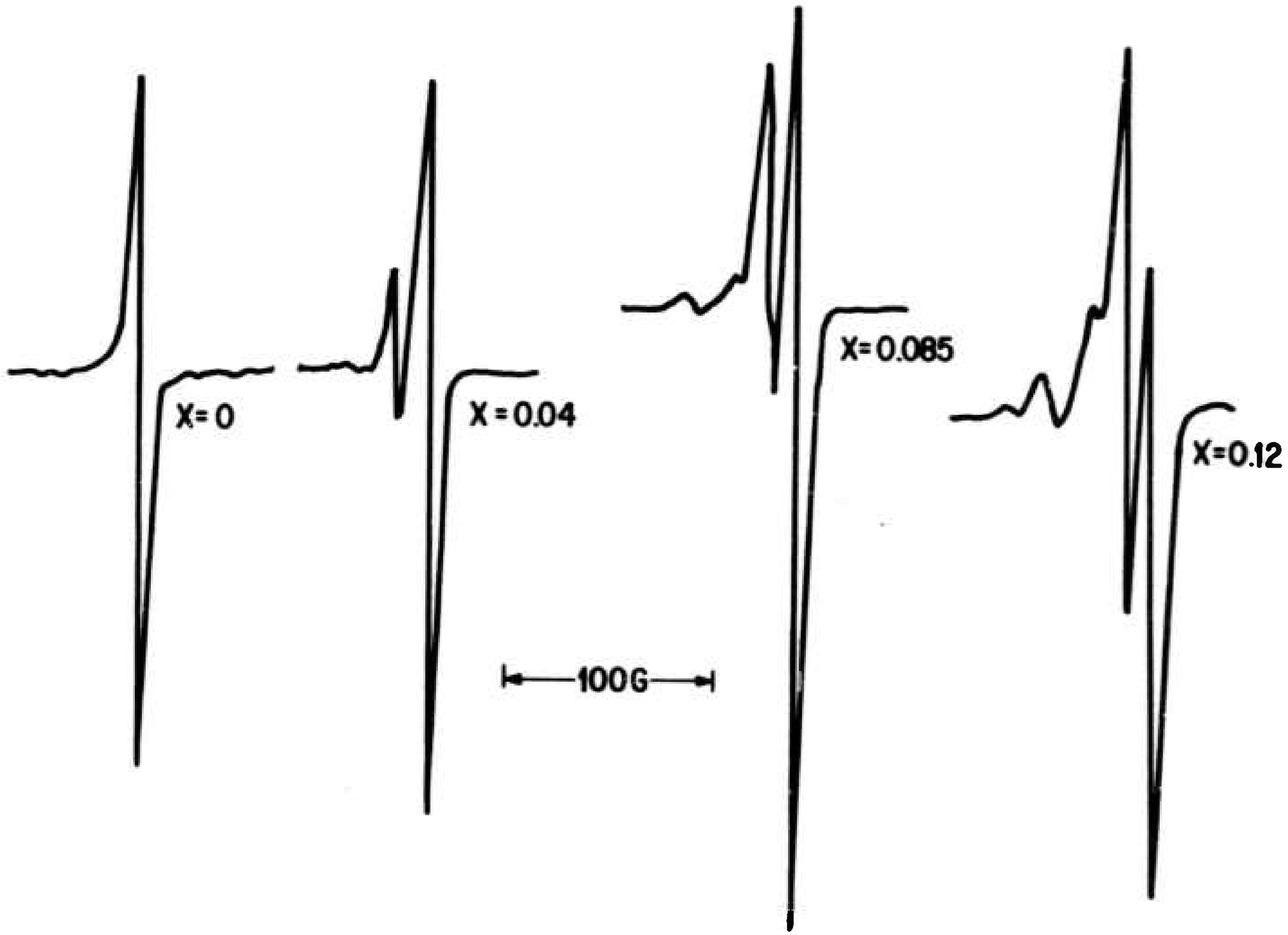

Figure 7 Low Field Resonance with the Field Along [001] (Marked g_z in Figure 11) for $Y_3Al_5O_{12}$ and Three Mixed Crystals. The satellite line, which grows with increasing x, is apparent. Other weaker structure also appears as x increases.

For the compositions x = 0.008, 0.04, 0.083, and 0.12, the ratio of the peak-to-peak derivative signal of satellite No. 1 to that of the main line for H || [001] is 0.063, 0.20, 0.37, and 0.89, respectively. (Satellite No. 2 contributes to the main line at this position.) For H || [110] where both satellites are well resolved from the main line, the lines are very broad and easily saturated, so that no reliable intensity measurements could be made at this orientation. The dependence of this ratio on Ga concentration is in agreement with simple statistical theoretical predictions for neither the Nd-1Ga nor the Nd-2Ga model. However, this is not unexpected. Nd^{3+} is a larger ion than Y^{3+}. Ga shows a preference for the tetrahedral sites[11] in $Y_3(Al_{1-x}Ga_x)_5O_{12}$, which decreases with increasing x, although Ga is larger than Al and the tetrahedral sites are smaller than the octahedral.

SECTION IV

CRYSTAL GROWTH AND CHARACTERIZATION

Crystal growth has emphasized the preparation of laser-size (0.6 cm dia x 7.5 cm) crystals of yttrium aluminum garnet (YAG), $Y_3Al_5O_{12}$ with varying amounts of gallium substituted for aluminum. Mixed garnet crystals, $Y_3(Al_{1-x}Ga_x)_5O_{12}$ (YAGG), with x = 0.1, 0.2, and 0.4, were grown. Nearly all crystals were grown with neodymium doping (YAGG:Nd).

At the time this work was initiated, YAG-Nd crystals of comparable size were available for laser use from several commercial suppliers. The purpose of this effort was therefore to proceed from existing YAG crystal growth technology and to develop a capability to grow mixed garnet crystals of sufficient size and optical quality for use as lasers. During the course of this effort, the YAG-YGG (yttrium gallium garnet) phase diagram was determined, the variation of the lattice parameter of YAG with up to 40% gallium substitution was measured, 14 crystals were grown for spectroscopic studies, 17 crystals were grown for EPR investigation, and 61 mixed garnet crystals were grown for laser rod preparation. In addition, several physical and mechanical properties of the mixed garnet crystals were determined and are presented in Section IV.B.

All crystal growth was carried out by the Czochralski method in a sealed chamber to permit control of the ambient atmosphere. The crystal growth program was organized so that pull rate, rotation rate, oxygen overpressure, initial melt composition, crucible size, and control parameters could be investigated individually as independent experimental variables.

A. Phase Diagram

Figure 8 shows the pseudo-binary phase diagram of YAG-YGG as determined in this study. Liquidus temperatures were measured using an optical pyrometer focused directly onto the melt. The solidus curve was calculated from the distribution coefficients as determined by chemical analysis of the first material

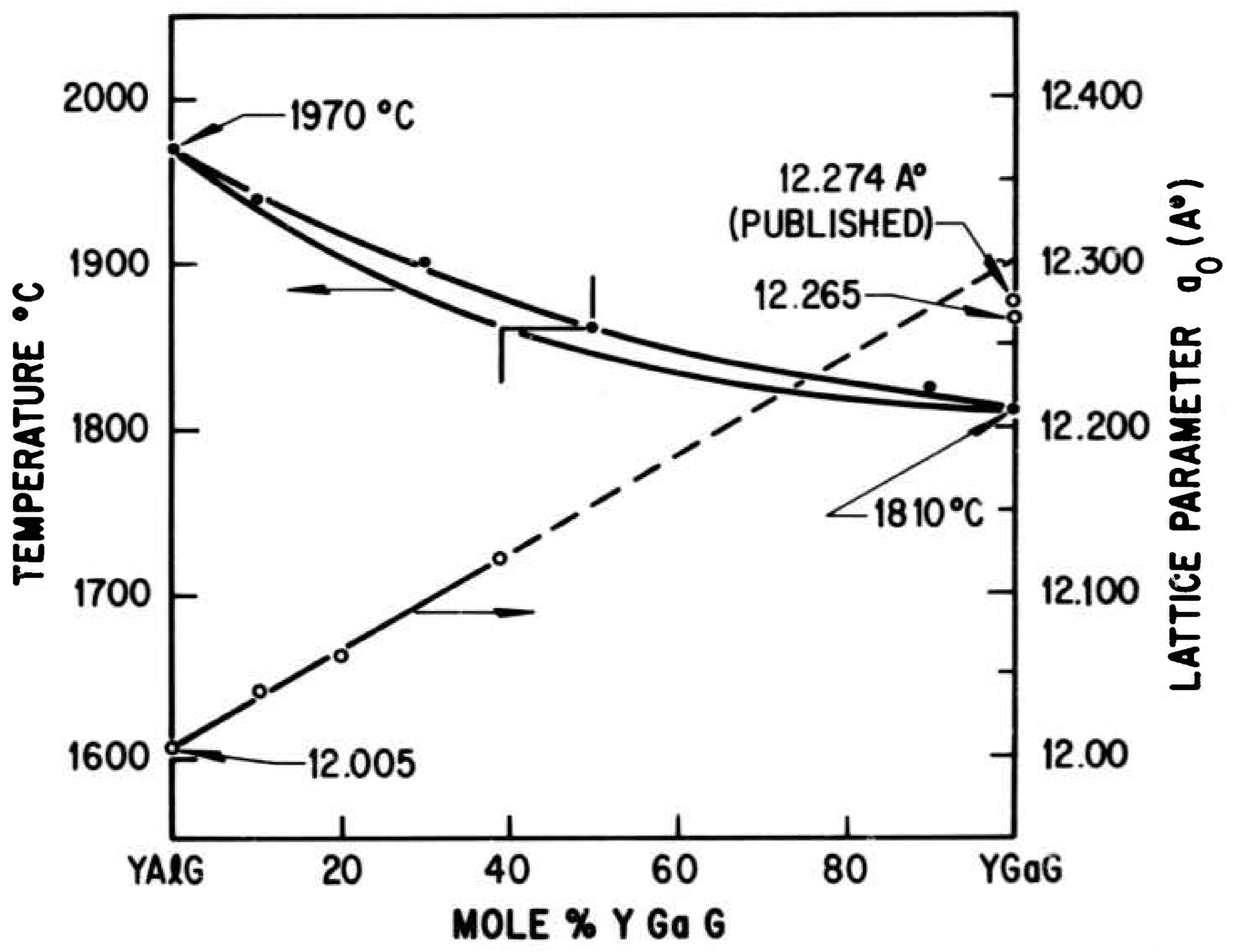

Figure 8 YAℓG-YGaG Phase Equilibria, Lattice Parameter

to solidify from a melt of known starting composition. It should be noted that the end members of this phase diagram are congruently melting compounds, but that the diagram itself is not a true binary system.

1. Distribution Coefficients

The effective distribution coefficients for Nd and Ga in the mixed crystal were calculated using chemical analysis data for the crystal top versus initial melt composition. These calculations show that k_{eff} (avg) for Nd in the mixed crystal is 0.23, and for Ga it is 0.75. The distribution coefficients are not constant, but vary with melt composition. In general,

(1) k_{eff} for Nd increases as the gallium content increases.

(2) k_{eff} for Ga increases as the gallium content increases.

The value of k for gallium approaches unity, of course, as the YGG content of the melt approaches 100%. For example, $k_{eff} = 0.95$ at 96% YGG and 0.86 at 80% YGG. This would make k_{eff} for aluminum in YAGG equal to 1.63 at 96% YGG and 1.5 at 80% YGG.

2. Lattice Parameter

Figure 8 shows that the lattice parameter of the mixed garnet obeys Vegard's law over the range investigated.

B. Material Sources

All materials used for crystal growth in this project were purchased in the form of sesquioxide powders. Rare earths were purchased from Research Chemicals, Phoenix, Arizona. Gallium and aluminum oxides were purchased from Johnson Matthey Chemicals, Ltd., through United Mineral and Chemical Corp., New York. Some gallium oxide was also obtained from Alusuisse Metals, Inc., Fort Lee, N. J.

C. Material Purity

All oxide powders were purchased as 99.999% pure. For the rare earths this number designates the purity with respect to other rare earths. Research Chemicals quotes an overall purity of better than 99.99% for its rare earth products. The aluminum and gallium oxides were generally Johnson Matthey Grade 1, which the supplier claims has an overall impurity content of less than 10 ppm by weight (99.999% pure). The gallium oxide obtained from Alusuisse Metals was quoted as 99.9999% pure.

D. Material Preparation

It was found that the optimum technique for preparing the starting materials was as follows. The precise amounts of each oxide needed for one run were weighed out and mixed thoroughly. The mixed powders were prereacted in air in a platinum crucible at 1200°C for about 18 hours. The reacted garnet powder was then melted into the iridium crucible in several stages. This procedure ensures that each melt contains the intended molar fraction of each constituent. In addition, presintering the starting powders drives off adsorbed water and carbon dioxide and generally results in a superior melt.

When a melt containing an excess of one or more constituents was desired, the stoichiometric melt was prepared as described above and the excess powders were added at the last crucible filling operation.

E. Crucibles

Iridium crucibles were used throughout this investigation. Crucibles were fabricated by the Baker Platinum Division of Englehard Industries, Blair, N. J. The most frequently used size was a 2 inch I.D. x 2 inch deep crucible with a wall thickness of 0.100 inch. Such a crucible would hold about 400 gms of melt.

Other crucible sizes used were a 1.5 x 1.5 inch crucible for the spectroscopic and EPR samples and a 2½ x 2½ inch crucible from which a number of large crystals were pulled.

F. Insulation

To achieve the desired melt temperature by induction heating it was necessary to insulate the crucible to reduce radiative heat losses. In general, two methods of insulation were used: (1) the crucible itself was insulated on the sides and bottom, and (2) a chimney was placed over the crucible to reflect heat radiated from the melt. Figure 9 shows the furnace design to scale. The basic insulation around the crucible was granulated ThO_2. This was thoria grog -14 to 28 mesh, purchased from Zirconia Corp. of America, Solon, Ohio. The thoria grog was contained in a recrystallized alumina muffle tube. Later, the alumina was replaced by a tube of ZIRCAR fibrous zirconia (3 inch I.D. x 4 inch O.D.) purchased from Union Carbide, Corp., Tuxedo, N. Y. This latter was a much better insulator.

Chimneys were made from castable zirconia (Zirconium Corp. of America) in a mold specifically designed for this program. Other insulation included Kaowool, a product of Babcock and Wilcox, Co., Richardson, Texas, and ZIRCAR felt (Union Carbide). Figure 10 shows the arrangement used to hold the seed crystal.

G. Atmosphere

All crystal growth was done in a flowing atmosphere of reduced oxygen content. The range of oxygen partial pressures from 0 to 5 volume percent was investigated. Both nitrogen and argon were used to make up the inert bulk of the atmosphere. From the crystal growth standpoint, the only advantage of argon over nitrogen is its lower thermal conductivity, which would further reduce power requirements to the crucible. However, argon is more prone to suffer arcing from the rf coil to ground; therefore, nitrogen was used predominantly in the later stages of research.

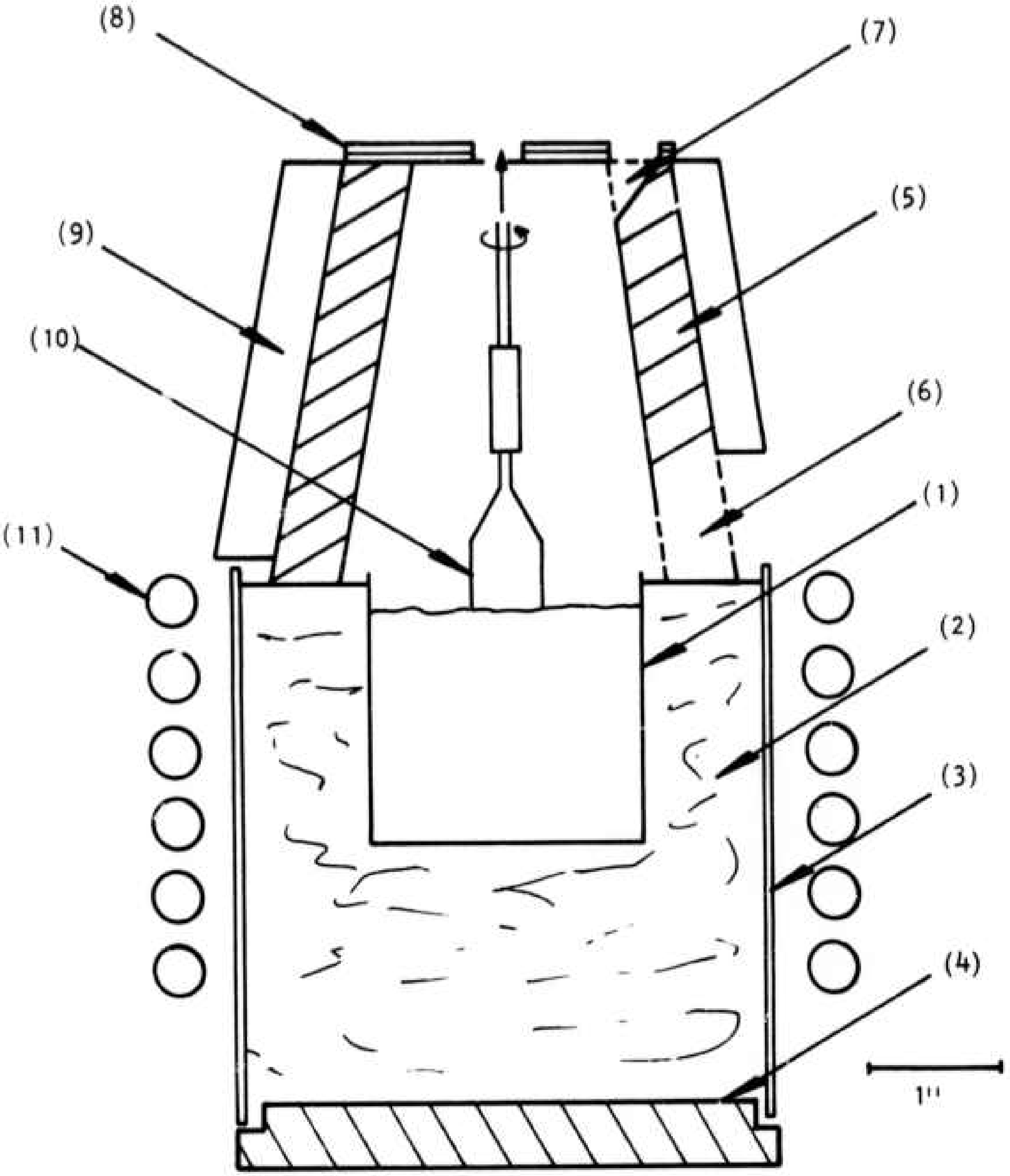

(1) Iridium Crucible Containing Melt
(2) Thoria Grog
(3) Alumina or ZIRCAR Cylinder
(4) Hewn Firebrick
(5) Castable Zirconia Chimney
(6) Operator's Viewport
(7) Viewport for Optical Control
(8) ZIRCAR Felt
(9) Kaowool Blanket
(10) Growing Crystal
(11) Induction Coil

Figure 9 Furnace Design

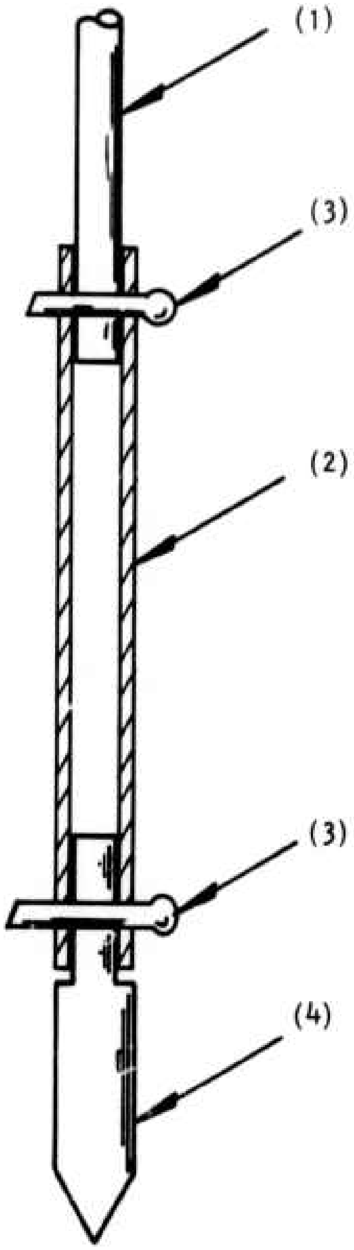

(1) Sapphire Rod
(2) Iridium Tube
(3) Iridium Pin
(4) Seed

Figure 10 Seed Holder

Flow rates from 100 to 5000 cc/min were used. The faster flow rates were investigated to ensure that the internal volume of the puller was flushed at a rate sufficient to keep pace with all possible oxidation/reduction reactions. In this way, the experimenter can be certain that the oxygen potential in the puller is that of the incoming gas mixture.

Gas mixtures were taken from three sources. Initially, premixed tanks were connected to the puller through a flow meter. Later, gas mixtures were made in situ by taking gas from tanks of pure nitrogen and oxygen and monitoring their flows through separate flow meters. Ultimately, the building gas supply was used. Nitrogen and oxygen from utilities within the laboratory were passed through filters to remove oil and water vapors and particulate matter as small as 12 μm in diameter, then through separate flow meters and into the puller.

H. Crystal Pullers

Two crystal pulling stations were used for most of the crystal growth. One consisted of a Lepel dual frequency 25 kW rf generator and an Arthur D. Little, Co. model MP crystal puller. This station is referred to below by the initials ADL. The other station (designated T-W) was powered by a Taylor-Winfield 60 kW rf generator, and the crystal puller was a custom-built apparatus using an Arthur D. Little pulling head for seed rotation and lift. This pulling head was in all essential respects identical to the one on the ADL. The estimated internal volumes of the pullers were 26 liters for the ADL and 45 liters for the T-W.

I. Growth Parameters

In the following sections the effect of each of the three main growth parameters on crystal quality is discussed.

1. Atmosphere

Since the constituents of the mixed garnet crystals are all oxides, some partial pressure of oxygen is required over them to prevent their reduction to the metallic state. The oxides of aluminum and the rare earths are extremely stable, and neodymium-doped YAG can be grown in an atmosphere that is nominally pure argon or nitrogen. The oxide of gallium is the least stable of the constituents, tending to reduce to a volatile sub-oxide through the reaction

$$Ga_2O_3 \text{ (solution)} \rightarrow Ga_2O(g) + O_2(g). \tag{15}$$

As this reaction proceeds, the gallium sub-oxide in the vapor phase condenses on the colder portions of the puller; thus, a stable level of gallium oxide is never achieved in the atmosphere, and the reaction continues until the melt is significantly depleted of gallia.

Two other reactions of importance occur in this system. They are the oxidation of iridium as

$$Ir + O_2 \rightarrow IrO_2 \text{ (vapor + solution)}, \tag{16}$$

and the reaction between gallia in solution and the crucible

$$Ga_2O_3 \text{ (solution)} + Ir \rightarrow Ga_2O \text{ (g)} + IrO_2. \tag{17}$$

At first glance reaction (17) appears to be merely the sum of reactions (15) and (16). However, it is significant to note that free oxygen does not appear in this reaction, and hence its rate is independent of the oxygen overpressure. Reaction (17) occurs at all oxygen pressures, therefore, and cannot be prevented.

Both reactions (15) and (16), on the other hand, contain oxygen gas and therefore are dependent on the partial pressure of oxygen in the puller chamber. To drive reaction (15) to the left as desired, an increase in oxygen potential is required. This, however, drives reaction (16) to the right, an undesirable consequence. Hence, a compromise must be struck in the choice of oxygen potential. The introduction of a soluble iridium oxide into the solution is not specifically detrimental to the growth of high quality crystals. However, as in the case of most noble metals, the oxide of iridium becomes less stable as the temperature is lowered. Therefore, in the vicinity of the growing crystal interface, the coldest part of the melt, free metallic iridium forms and is incorporated as a precipitate into the growing crystal.

Oxygen potentials in the range of zero to five volume percent were investigated, with most of the effort centered around two percent.

2. Pull Rate

The rate at which the crystal is pulled from the melt can have a significant effect on its optical quality. The growth rate is essentially the same as the pull rate, except that the melt drop adds an additional amount. In pulling a crystal of diameter d from a crucible of diameter D it can be shown that the true growth rate G is given by

$$G = (P - L)\left(1 + \frac{\alpha d^2}{D^2}\right), \tag{18}$$

where P is the pull rate, α is a factor depending on the solidification shrinkage, and L is the crucible lift rate. In this investigation programmed crucible lift was never used, so L is always zero. Also, the solidification shrinkage can be ignored, so α is unity. Thus,

$$G = P\left(1 + \frac{d^2}{D^2}\right). \tag{19}$$

For a typical crystal $d \approx 1$ inch and $D = 2$ inches, so the growth rate is up to 25% faster than the pull rate. The pull rate will be given as the experimental variable. Pull rates between 0.25 and 1.1 mm/hour were employed.

In general, slower growth rates result in crystals of higher optical quality.

3. Rotation Rate

In Czochralski growth the seed and the crucible are usually rotated to even out radial temperature inhomogeneities. This keeps the thermal center of the system at the geometrical center of the crucible and keeps the crystal growing evenly. For this project crucible rotation was not used. Crystal rotation rates between 6 and 66 rpm were studied.

The mixed garnet, like YAG, grows with $\{211\}$ type facets. These facets are supercooled with respect to the freezing isotherm and therefore grow in a high defect level. This leads to a core region with a high dislocation density unsuitable for optical uses. It is a well-known fact that fast rotation rates produce flat solid-liquid interfaces and eliminate coring. We therefore extended our investigation of rotation rates to include this effect.

J. Control

Temperature control is of paramount importance in Czochralski growth. This section contains a description of the techniques by which control parameters were selected to achieve optimum crystal growth. The control problem can be approximately separated into two regimes: a short-term cycle when temperature excursions occur on a time scale much less than the overall time necessary to grow a crystal, and a long-term part wherein temperature variations occur with a frequency of the order of the overall crystal growth operation. Since 7.5 cm crystals were desired and pulling speeds of 0.5 mm/hour were utilized most frequently, the total time needed to pull a crystal was 150 hours, or about six days. Thus, long-term control was needed to cope with two distinct problems: (a) the gradual emptying of the crucible and consequent change in thermal geometry, and (b) diurnal changes in both city power supply and room temperature. The short-term control corrected for momentary changes in building power caused by the startup of heavy equipment or lightning storms and random thermal fluctuations in the crucible.

1. Power Control

Constant power to the crucible was the first and most basic control method applied. A pick-up coil was placed around one lead from the rf generator. The induced current in this coil (~ 100 V, 450 kHz) was rectified, filtered, and attenuated to a dc signal of about 50 mV. This signal was fed into a Leeds and Northrup "AZAR" proportional controller. The proportional controller, using an operator-selected set point, produced a 0 to 5 mV error signal which went into the thyratron controller of the rf generator. (The AZAR controller was used throughout this project as a proportional controller.) Although this technique (constant power) is simple, reliable, and has a rapid response, it does not solve the basic control problem, that of maintaining a reasonably constant crystal diameter over the long crystal growth run. Its best feature is that it rapidly compensates for short-term disturbances. To correct for large-scale, long-time changes in diameter, a motor driven potentiometer was inserted into the set point circuit. The operator could then drive the set point up or down at a rate determined by visual inspection of the growing crystal. This method relies heavily on experience and is severely hampered by the slow growth rate, which does not allow for a positive feedback of the rate and direction of change of crystal diameter in a reasonable time period.

2. Optical Diameter Control

An IRCON model 2000 infrared sensor was used to provide a control system with a more positive diameter control. This device detects the temperature of a small area (~ 1/8 inch dia) and produces a proportional dc millivolt output. The output of the IRCON was used as the input to the AZAR for control as with constant power. The optical system of the IRCON enables the operator to visually select the area in which temperature is to be monitored. For control, three areas were used: (1) the crucible wall, (2) the melt surface, and (3) the meniscus at the edge of the growing crystal. All areas gave good response for feedback control, but only the last two gave good diameter control. The most serious drawbacks to this technique were the lag in response due to the large thermal inertia of the system and the random noise caused by convection currents in the melt. The latter was eliminated by increasing the time constant of the instrument. Also, the meniscus temperature for the mixed garnet was not significantly higher than for the surrounding melt. Thus, it was not possible to develop as strong an error signal for control as that found for pure YAG, for instance.

K. Results

The following sections include a compilation of the crystals grown for the various phases of the program and a description of the principal defects observed in these crystals.

1. EPR Samples

A series of small (30 to 50 g) crystals was pulled with $\sim 10^{18}$ cm^{-3} Nd^{142} doping for electron paramagnetic resonance experiments. Since large size and high optical quality were not criteria, a relatively fast pull rate (4 to 5 mm/hour) was employed. These crystals were pulled from a 1.5 inch dia x 1.5 inch iridium crucible using a furnace design similar to that described previously in this section. The series included compositions from pure YAG in steps to pure YGG.

2. Spectroscopic Samples

A second series of small crystals was pulled for spectroscopic studies. This series also spanned the composition range from pure YAG to pure YGG. The neodymium content of these crystals was varied from about 0.1 to 1% of the total rare earth. The crystals were pulled from a 2 inch x 2 inch iridium crucible, as were the laser-size crystals.

3. Laser Crystals

Sixty-one boules were pulled for laser rod fabrication. These included crystals in the composition range from pure YAG to 40% YGG. All were doped with neodymium except for a few YAG crystals grown to de-bug the automatic diameter control. About half these crystals contained 40% gallium substitution. Of the remainder, the largest number contained 10% gallium substitution. Typical crystals are shown in Figures 11 and 12.

4. Defects

The crystals pulled for this contract have shown five major types of defects: cracks, iridium particles, gas bubbles, striae, and precipitates. The precipitates may include both impurity particles and second phase oxides. Each type of defect is correlated below with the growth parameters that cause it, and the experimental procedure used to eliminate it is defined.

(1) Cracks can be correlated with extreme variations in crystal shape in nearly every instance. Such shape variations can be described simply as too rapid a change in diameter for a particular length of pulled crystal. Since this effect corresponds to a marked variation in growth rate, regions of pronounced shape change may well be full of the various local defects listed above, and these defects may serve as nucleation sites for cracks. Alternatively,

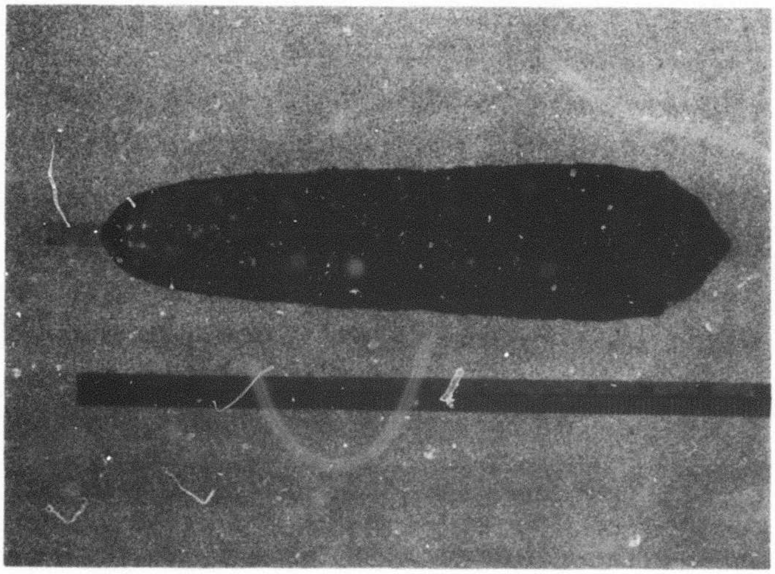

Figure 11 YAGG #24

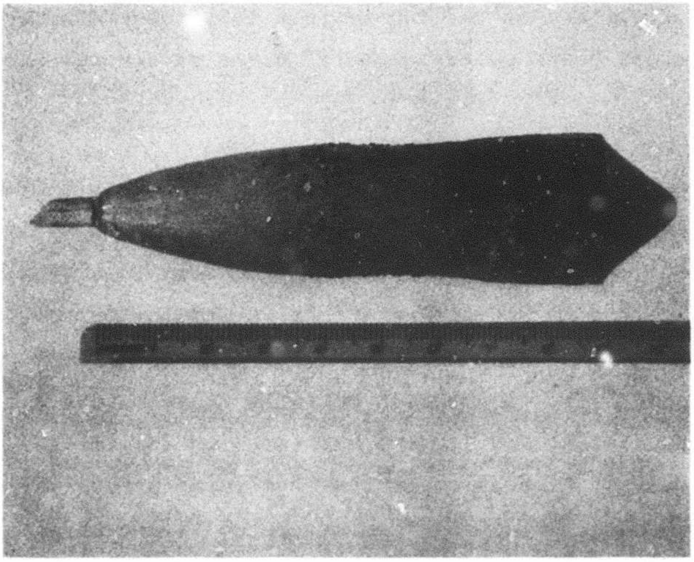

Figure 12 YAGG #23

cracks may result from differential thermal stresses in these regions. In any event, precise diameter control should lead to a reduced number of cracks. The results of crystals grown using automatic diameter control support this contention.

(2) Gas bubbles are almost certainly the result of oxygen evolution at the melt-solid interface. A possible reaction is $IrO_2 \rightarrow Ir + O_2$ (g). (Iridium is the only metal in the system whose oxide becomes less stable as temperature decreases. Since the solid-melt interface is the coldest portion of the melt, iridium oxide that has formed in other parts of the system would decompose here, liberating oxygen.) It has not been possible to establish a one-to-one correlation between gas bubbles and iridium particles in the crystal, but the bubbles seem closely tied to the thermodynamics of iridium accumulation in the melt. Figure 13 shows the gas bubbles are distributed in two ways. Toward the top of the crystal they are evenly dispersed across the crystal diameter [Figure 13(a)]. This distribution occurred mainly in the conical part of the crystal where the diameter was increasing with time. Along the remaining length of the crystal the bubbles occupy a well-defined region just under the surface. The reason the bubbles are restricted to this surface region is not known.

(3) Iridium is present in the system in two regimes of interest: as a soluble oxide in the melt and as an insoluble metal floating on the surface. It is reasonable to argue on thermodynamic grounds that these regimes are mutually exclusive, since for a given oxygen potential only one of the two species (metal or oxide) will be stable. (This is strictly true, though, only for an isothermal system.) From a crystal-growing point of view it is desirable to lower the oxygen potential and encourage formation of the metal on the liquid surface. This removes the metal from solution in the melt and should prevent the occurrence of iridium particles within the crystal. These particles are

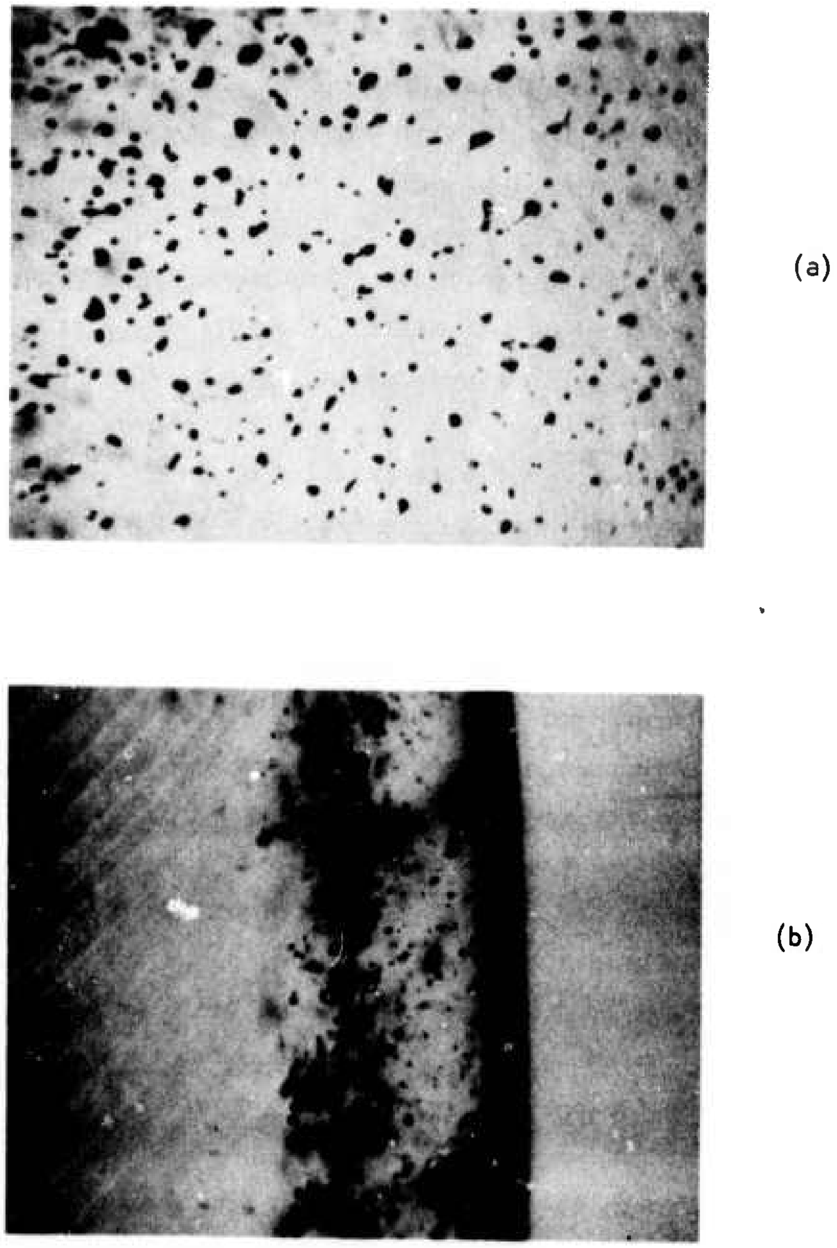

Figure 13 (a) Bubbles in Top Section of YAGG-50 (32X); (b) Bubbles and Precipitates Under the Surface of YAGG-50 (32X).

singularly destructive to laser operation. However, a large pool of iridium on the melt surface makes the initial dipping of the seed crystal almost impossible. It also prevents a clear sight path to the melt for optical control.

In addition to controlling the iridium transfer into and out of the melt, the oxygen potential affects the rate of gallium loss from the melt through the reaction which forms a volatile sub-oxide [Ga_2O_3 (solution) → Ga_2O (g) + O_2 (g)]. However, an investigation of the thermodynamics of this reaction indicates that at the temperature of interest the equilibrium oxygen potential is much less than 1%. In fact, it has been reported that the rate-controlling factor for this reaction is the precipitation of solid Ga_2O from the vapor phase in the colder parts of the puller.

In addition, the kinetics of iridium oxidation in such a massive system cannot be ignored. If an initial level of iridium has been established in the melt during the crucible loading procedure, this iridium can only be removed at the melt surface. And it has been reported that equilibrium between melt and vapor phase may take as long as eight hours in similar systems. It is also generally assumed that there is a continuous reaction between gallium oxide in the melt and the iridium crucible [Ga_2O_3 (solution) + Ir (solid) → Ga_2O (g) + IrO_2 (solution)] which results in a continuous introduction of iridium into the melt independent of oxygen overpressure.

(4) Growth striae are clearly a significant problem. They are due to temperature fluctuations in the melt, although secondary sources can be variations in the pull rate brought about by mechanical stability problems in the pulling head and power fluctuations. Significant improvements have been made in the micro-structure of the crystals with regard to striae by stabilizing the power supply, but clearly these have not been enough. The crucible temperature follows the power input quite closely, but it is not readily apparent how

long it takes the melt to reestablish equilibrium after a variation in the power level is introduced by the controller. Neither is it a priori a fact that once a deviation has occurred and been corrected and the original power level restored, the melt temperature will return to the same value. Photographs of striae in three crystals are shown in Figures 14 through 16. Several significant features can be observed. In Figure 14 the striae are spaced with remarkable uniformity. Figure 17 is a histogram showing that the spacings between points A and B are grouped around a common value corresponding to about 27 minutes. The striae of YAGG-34, Figure 16, were observed to have two peaks of preferred spacings (Figure 18) superimposed on a background of spacings of decreasing frequency (perhaps random). Figure 15 shows the striae of crystal 46. The significant feature here is the wide spacings in time over which some striae extend. These would seem to indicate a slow return to equilibrium on the part of the melt after a momentary power fluctuation. The macrograph in Figure 15 shows heavy striae marked on each side of the crystal. The striae on each side are spaced at about 24 hour intervals, and the two sets are about 8 hours apart. These striae clearly arise from diurnal power fluctuations.

(5) Precipitates are both a thermodynamic and a control problem. Their origin can be purely thermodynamic (e.g., nonstoichiometry), or they can be caused by the sudden unbalance of equilibrium due to a controller excursion. If the point defects are of thermodynamic origin, they should be fairly evenly and randomly distributed throughout the length of the crystal. If they arise from a controller dysfunction, however, they should be highly localized within the crystal. The appearance of localized defects in YAGG-48, discussed below, points to controller dysfunction as the source of the problem. Still, thermodynamics is involved in the creation of the stria, since a considerable amount of iridium was in the melt at the time the supposed control instability occurred.

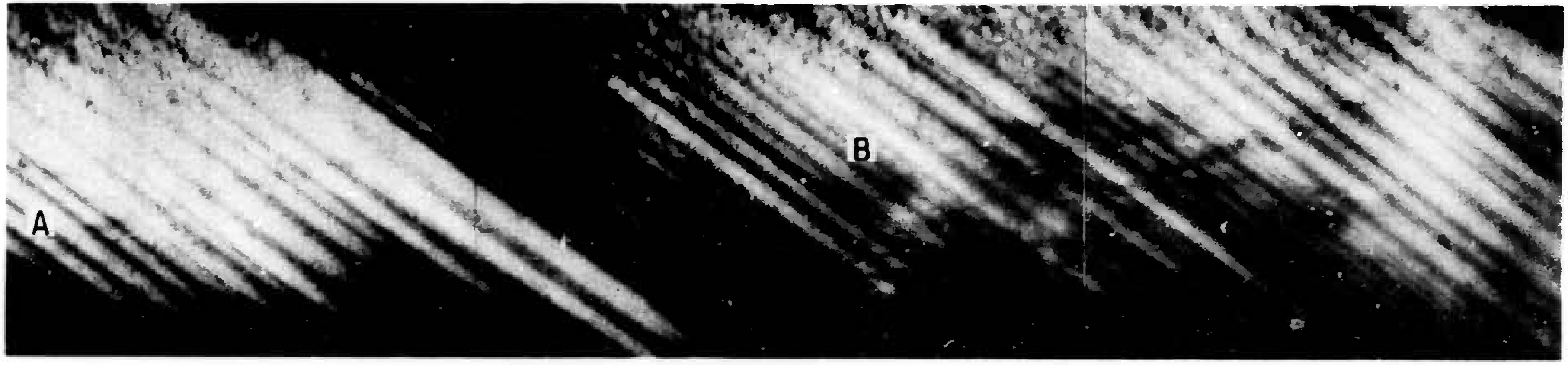

Figure 14 Striae in Crystal YAGG-40 Photographed Through Crossed Polarizers

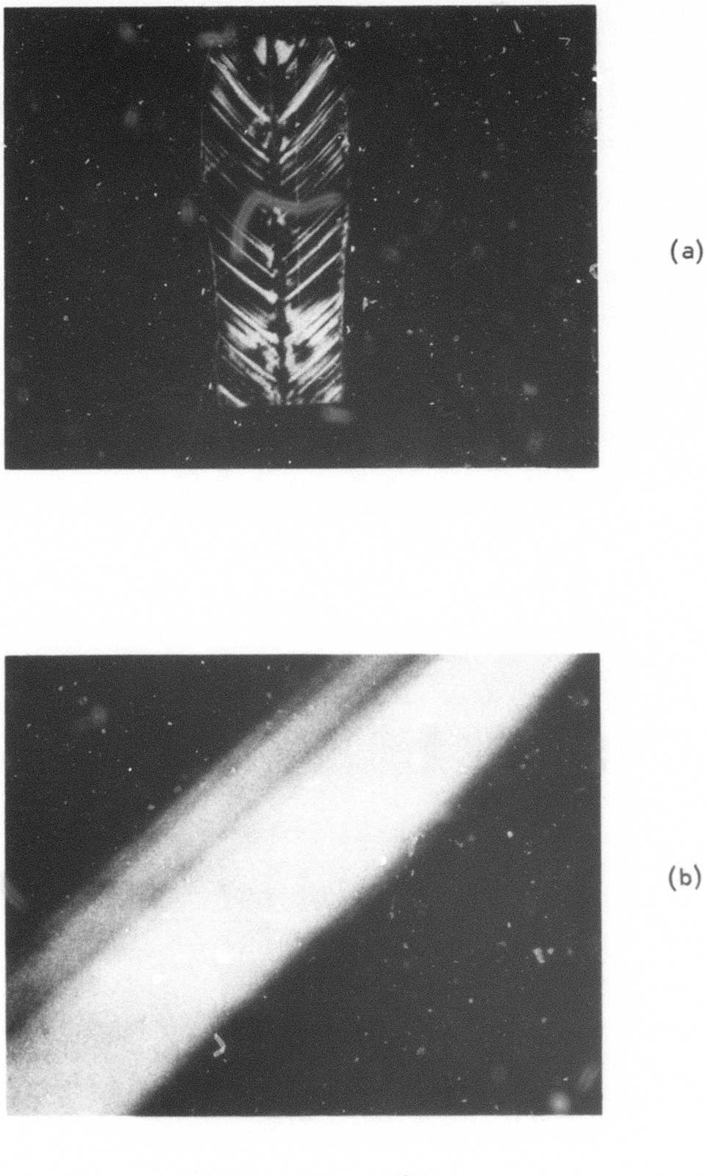

Figure 15 (a) Section Through YAGG-46. (b) Detail of a Heavy Stria. Both photographs made through crossed polarizers.

Figure 16 Striae in YAGG-34

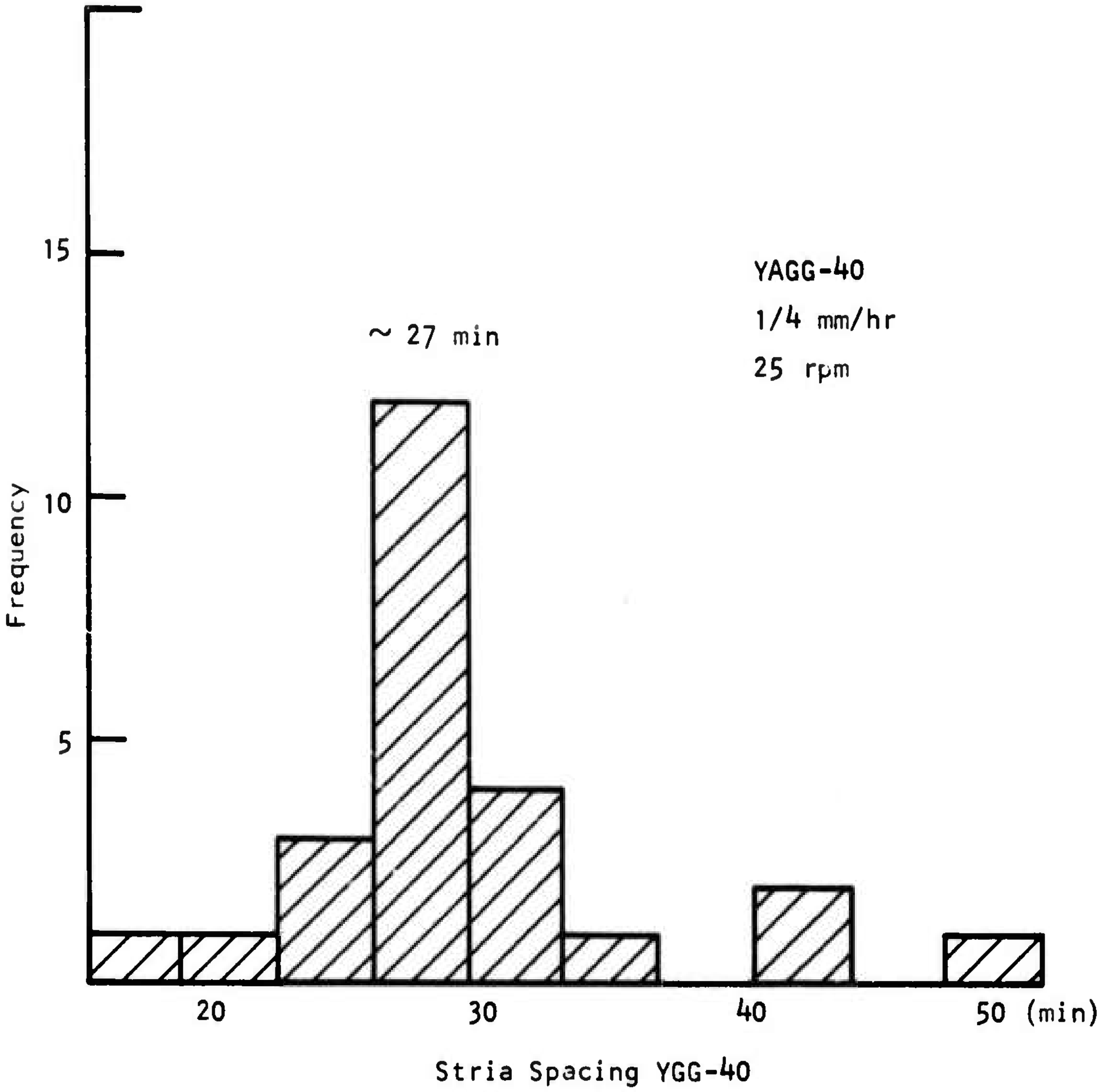

Figure 17 Stria Spacings in YAGG-40

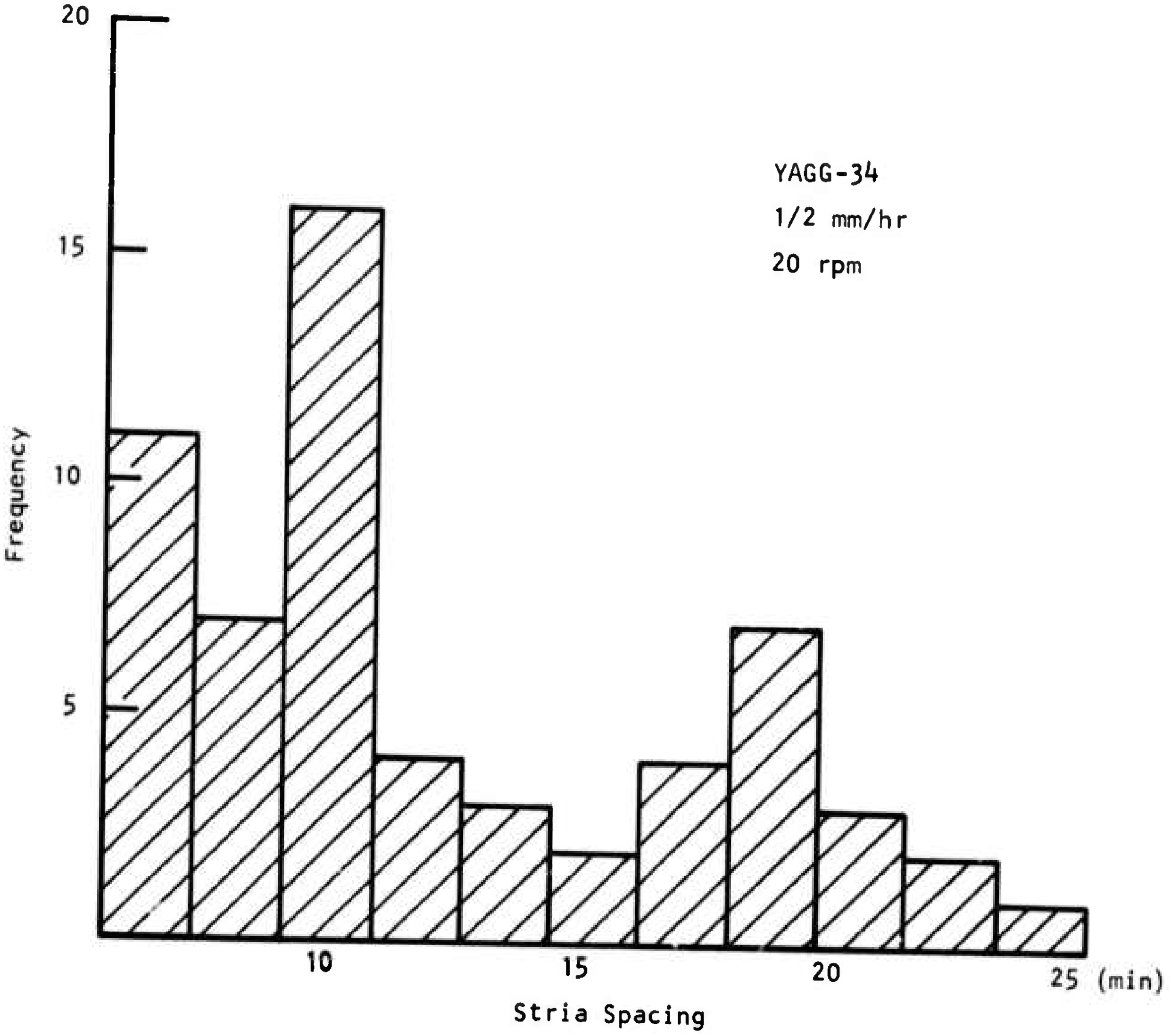

Figure 18 Stria Spacings in YAGG-34

Two views of YAGG-49 are shown in Figure 19. This crystal, grown with automatic diameter control, shows several pronounced growth striae and a region of cross-stria, strain lineage about two-thirds down the length when the crystal is viewed through crossed polarizers. However, when a laser beam is transmitted down the length of the rod, the principal defects appear to be a few striae heavily decorated with small defects. Figure 20 shows a number of views of the crystal near one of these striae. Figure 20(a) shows the core region (right) with several large iridium particles and one of the striae (upper left). The particles on the stria are much smaller than those in the core. Figure 20(b) shows the highly localized nature of the stria. The surrounding crystal is virtually free of point defects. Figures 20(c) and (d) are views of this stria at higher magnifications. In these four photographs three defect morphologies, triangles (iridium), spheres (bubbles) and rods (second phase precipitates ?), can be distinguished. It is conjectured that a momentary control malfunction produced this highly localized stria in an otherwise perfect crystal. Both the limited extent of the defects and their size suggest this possibility. Defects formed rapidly, as in the sudden forward movement of the solid-melt interface, tend to be smaller than those formed under conditions of equilibrium such as the large ones in the lower part of the core region in Figure 20(a).

L. Discussion

All but two of the four defect types discussed above can be linked to control problems. Gas bubbles and iridium are of thermodynamic origin, as well. The control problem is twofold. Because of the slow pull rate required to produce a useful length of crystal (at least seven days) long-term control of crystal diameter is necessary. Precise diameter control also fixes the growth rate of the crystal and hence the rate at which defects are produced. This helps determine the optimum growing conditions for defect elimination. Some

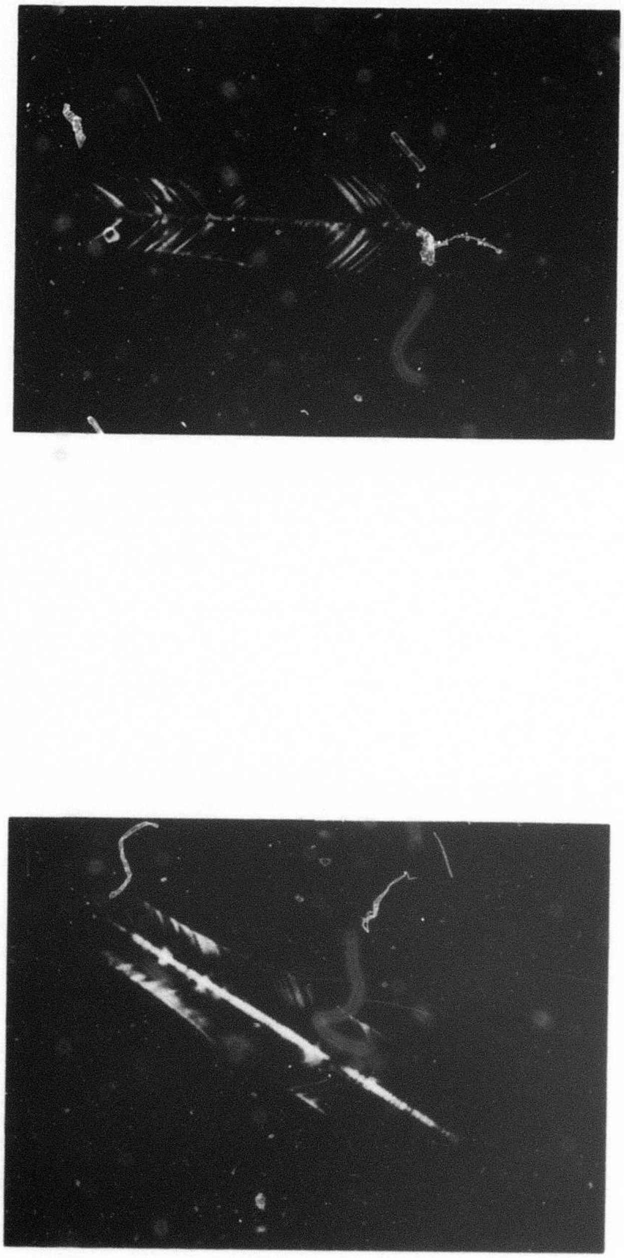

Figure 19 Two Views of YAGG-49 Through Crossed Polarizers. (Approximately actual size.)

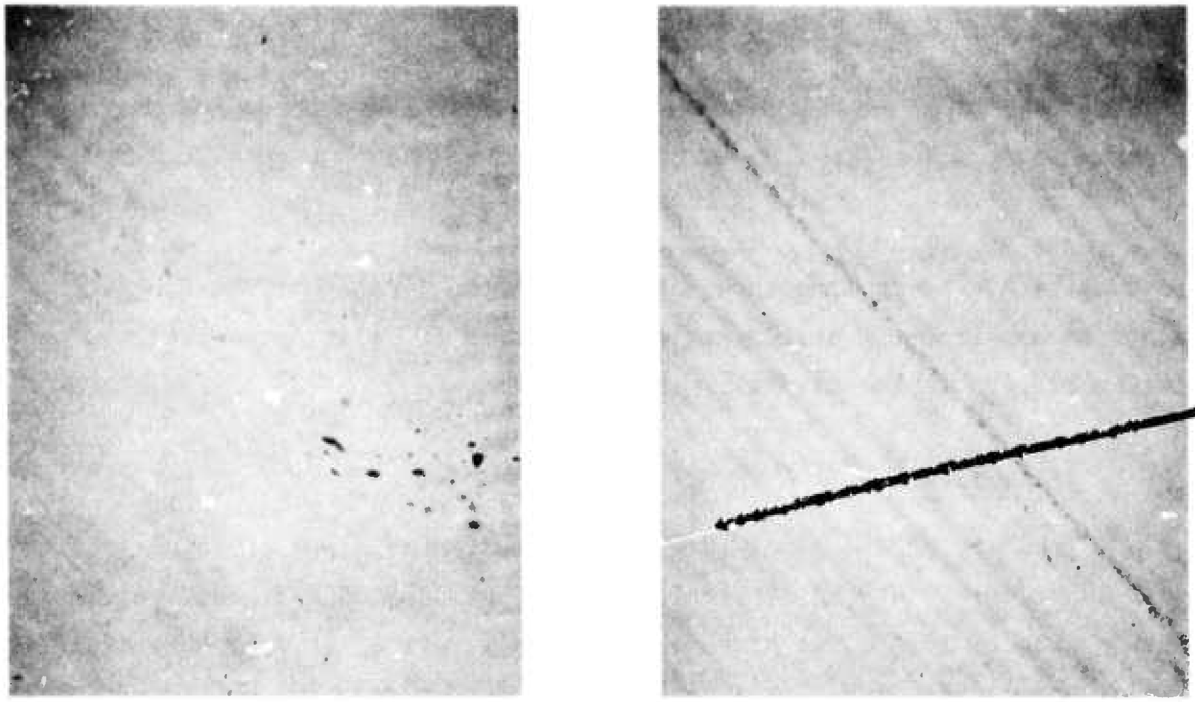

(a) Core region and part of one stria. (80X)

(b) Heavy growth of precipitates and bubbles along a stria. (80X)

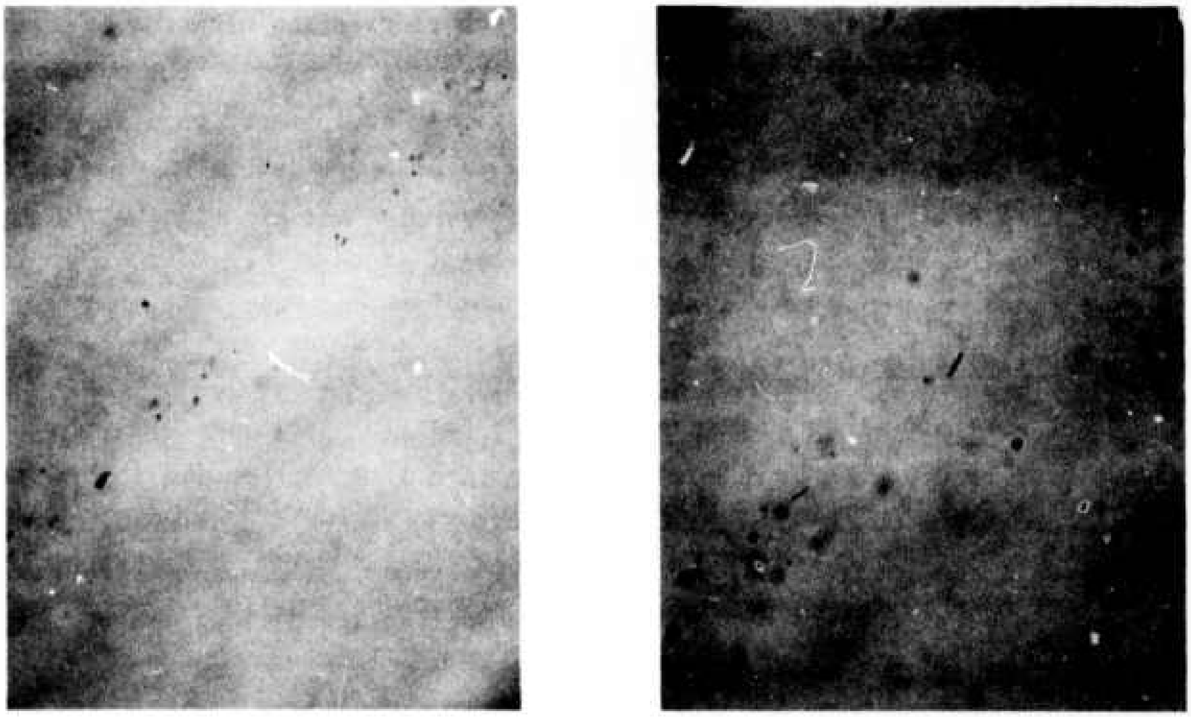

(c) Enlargement of (b). (160X)

(d) Enlargement of (b) showing rod-shaped precipitates. (360X)

Figure 20 Views of YAGG-49, Transmitted Light [illegible]ccess was achieved in long-term control with the Ircon controller. Below, some of the experimental parameters are discussed in relation to their role in defect production in the crystal.

1. Atmosphere

The role of the atmosphere in the pulling of mixed aluminum-gallium garnets is crucial. At the temperatures involved (1850°C and greater) the oxidation rate of iridium is high. The boil-off rate of Ga_2O is also significant. A high oxygen partial pressure suppresses the latter reaction while exacerbating the iridium oxidation. The optimum compromise for this system is in the range of 2 to 3 vol % oxygen. However, even at this level, losses of gallia still occur.

One factor that must be noted in this context is the rate of flow of gas mixture into the puller chamber. In addition to reacting with the melt and crucible, the gas components react with each other. (The odor of the oxides of nitrogen is readily noted on opening the puller chamber.) Thus, to assure the desired gas mixtures in the puller, rapid flow rates are essential. Flow rates as fast as 5 liters/min were used in this program. The use of argon as the inert constituent of the atmosphere would circumvent this problem.

2. Pulling Rate

It was found that the optimum pulling rate for the mixed garnet was in the range 0.25 to 0.6 mm/hour. Speeds greater than 1 mm/hour caused the formation of an excessive number of optical defects. The number and severity of striae seemed to be largely unaffected by pulling speed. Since very little improvement in crystal quality was realized with pulling speeds lower than 0.5 mm/hour, this would seem to be the optimum value.

3. Rotation Rate

Like YAG, the mixed garnet grows with a faceted interface, the facets being {211} planes. It is a well-documented fact that at fast seed spin rates the solid-liquid interface can be made to go flat, eliminating the facets and the associated core region. Figure 21 shows the effect of rotation rate on interface flatness at low spin rates. The apex angle was the included angle between growth striae measured on an axis slice of the crystal. At faster spin rates, however, the interface does become flat and the crystal grows without a core. Several of the last crystals pulled were rotated at 66 rpm and were core-less when later examined. However, the severity of their striae was not appreciably different from that of crystals grown at lower spin rates. Figure 22 shows a view of such a crystal through crossed polarizers.

4. Control

Precise control of the melt temperature is essential in Czochralski growth. In this program the two major types of control used were constant power and optical diameter control, as discussed above. The major drawbacks of the constant power controller were that: (1) the diameter of the crystal varied considerably as the melt level dropped and the thermal geometry of the crucible changed, and (2) power line and room temperature fluctuations were not filtered out by the controller. Figure 23 shows the variation in crystal diameter caused by the effect of diurnal variations of room temperature on the controller electronics package. This feature was eliminated by placing these components in a constant-temperature oven. Diurnal fluctuations in city power also appeared in crystals as pronounced striae. These were eliminated in one case by connecting the input of the rf generator to the output of a motor-generator set which isolated the rf generator from city power fluctuations.

The optical diameter control as used here did not function as expected, largely because of the long lag between feedback and response caused by the large

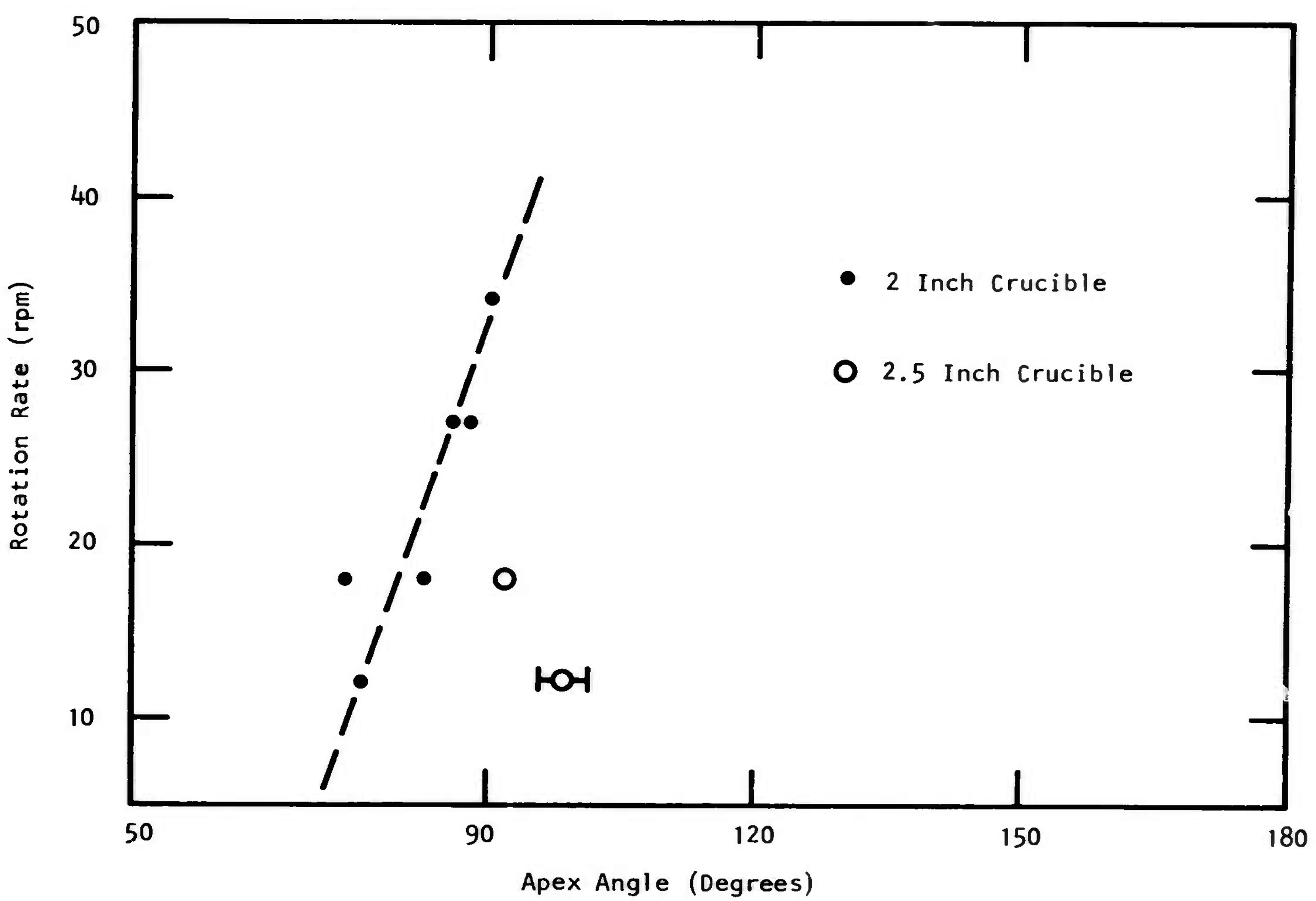

Figure 21 The Effect of Seed Rotation Rate on Interface Shape. Included angle between striae plotted vs rotation rate for crucibles of 2 and 2.5 inch diameter.

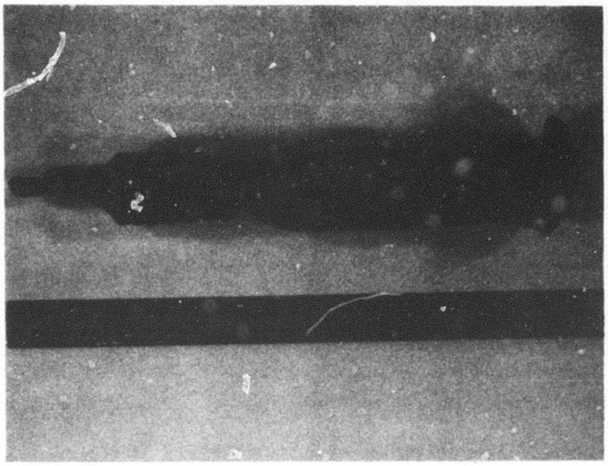

Figure 22(a) YAGG-59, As-Grown

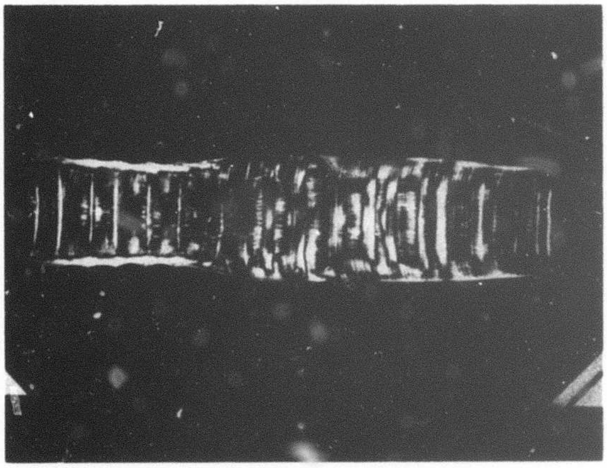

Figure 22(b) Viewed Through Crossed Polarizers. Note flat striae and lack of core. Approximately actual size.

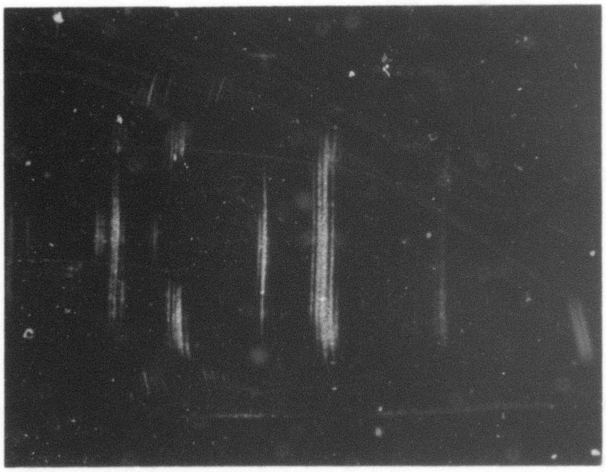

Figure 22(c) Bottom Section of YAGG-59. Approximately 3X.

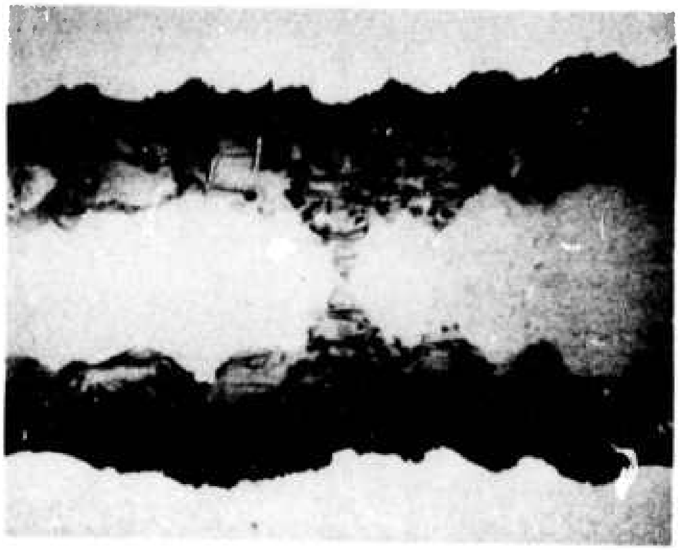

Figure 23 YAGG No. 19 Showing Diameter Variations

thermal inertia of the furnace. This technique also relies heavily on a pronounced meniscus temperature to provide a strong error signal when the crystal diameter varies. The mixed garnet seemed to lack this; consequently, this form of diameter control was only partially successful.

M. Conclusions and Summary

Pulling mixed $Y_3A\ell_5O_{12}$ - $Y_3Ga_5O_{12}$ crystals from the melt creates an extremely harsh environment (1800 to 1900°C, oxidizing atmosphere for eight days) and leaves little choice of materials suitable for the task. Although considerable success was achieved in the crystal growth aspect of this program, large sections of garnets were not grown with the low optical defect count required for laser rod fabrication. This failure can be traced to a few critical system parameters.

- Crucible Material

In any crystal growth operation it is an absolute prerequisite that the crucible material be inert with respect to the melt. This is rarely the case with oxide melts and noble metal crucibles, but these are the only crucible materials available. The use of iridium in the temperature and oxygen potential range required for these mixed garnets was totally unsuitable. It is doubtful that a group of experimental variables could ever be found that would reduce the attack of the crucible and incorporation of iridium particles in the crystal to an acceptable level.

- Phase Diagram

The large separation between the solidus and liquidus temperatures in this system and the lattice parameter variation lead to an inherent problem of growth striations. These are an obvious optical defect. Due to random thermal fluctuations caused by convection currents, it is probable that even the most carefully designed controller would not be able to eliminate the growth striae completely.

- Components

Great difficulty is always encountered in growing crystals from a melt that contains a volatile component. Although rare-earth gallium garnets can be grown with ease at lower temperatures, the evaporation rate of gallia from the mixed garnet melts was severe, largely because of the higher temperature.

- Recommendations

It is therefore recommended that further work on the growth of optically clear, neodymium-doped, mixed YAG-YGG crystals be discontinued. Mixed rare-earth aluminum/gallium garnets whose melting points lie below about 1700°C and whose phase diagrams suggest a closer solidus-liquidus separation may be much more likely candidates for high quality crystals.

SECTION V

PHYSICAL PROPERTIES MEASUREMENTS

One of the main advantages of YAG is its superior physical properties with regard to thermal conductivity, hardness, and thermal expansion. A main concern in the growth of the mixed garnets is how severely these properties are degraded by the addition of gallium in the garnet crystal. In this study five physical parameters were measured: thermal conductivity, thermal expansion, unit cell size, microhardness, and index of refraction.

Room temperature thermal conductivity measurements were made on several specimens at Texas Instruments using a McClure Park Corp. thermal comparator and by Dynatech, Inc., using a Colora Thermoconductometer. Additional measurements at 167°C were made on the Colora Thermoconductometer. The data are shown in Figure 24 and in Tables III and IV. The samples were (1) a piece of pure YAG grown at Texas Instruments; (2) two pieces of Nd:YAG, one grown at TI and one commercial piece (Airtron); and (3) several pieces of Nd:YAGG with nominal 10, 20, and 40% gallium substitution. The data suggest there is a rapid decrease in thermal conductivity with small additions of Ga to YAG, followed by a gradual further diminution as the gallium substitution increases.

Measurements of the linear thermal expansion of the mixed crystals were conducted on a fused quartz LVDT equipped dilatometer designed and constructed at Texas Instruments. The unit has a sensitivity of 1×10^{-6} inch. The expansion was in the [111] direction and was measured over a temperature range of 25°C to 500°C. A graph of thermal expansion vs composition is shown in Figure 25, and the data are summarized in Table V. The value for pure YAG agrees with the published value of $6.9 \times 10^{-6}/°C$.[12] The data indicate the same behavior pattern as the thermal conductivity. A small addition of gallium causes a rapid increase in the thermal expansion, followed by very gradual increases with further gallium additions.

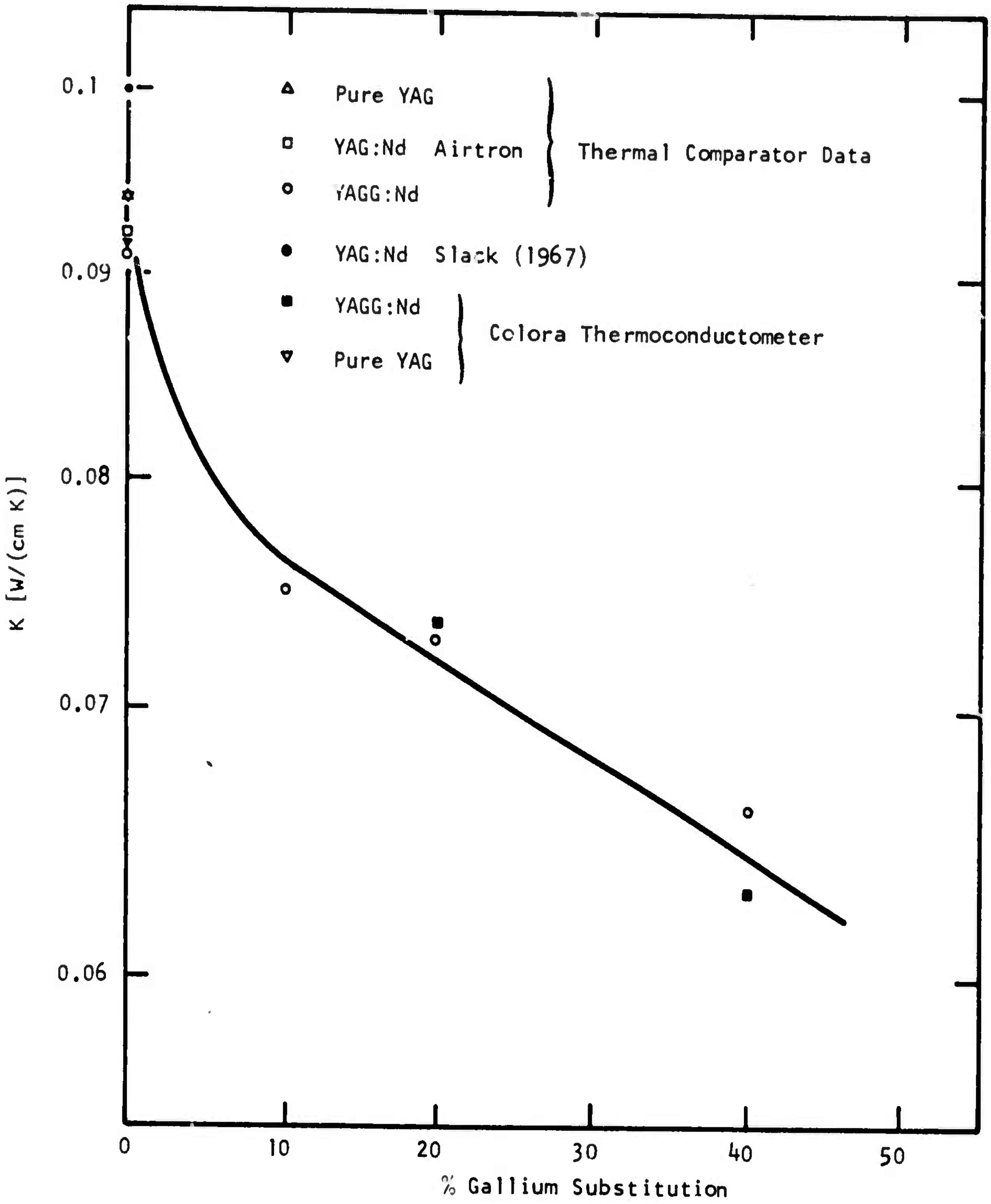

Figure 24 Thermal Conductivity of Gallium Substituted YAG Crystals as a Function of Gallium Content

TABLE III

THERMAL CONDUCTIVITIES (W/cm K)

Sample	By Thermal Comparator	By Colora Thermoconductometer	Others	
YAG	0.094	0.094		0.123(1)
YAG:Nd	0.091		0.100(3)	0.130(1)
YAG:Nd*	0.092			
YAGG:Nd 10% Ga	0.075	0.0735		
YAGG:Nd 20% Ga	0.073	0.074		
YAGG:Nd 40% Ga	0.066	0.063		

---

*Airtron

(1) Klein and Croft (1967)
(2) Previous measurements, this project
(3) Slack (1967)

TABLE IV

THERMAL CONDUCTIVITIES MEASURED BY COLORA THERMOCONDUCTOMETER

Sample No.	Composition	Thermal Conductivity ($W\ m^{-1}\ k^{-1}$)	
		40° C	167° C
YAG-17	Pure YAG	9.1	7.4
YAG-17	Pure YAG	9.1	7.4
YGG-17	10% Ga	7.3	6.4
YGG-17	10% Ga	7.4	6.5
YAG-1	Pure YAG	9.4	7.1
YGG-40	40% Ga	6.3	5.2

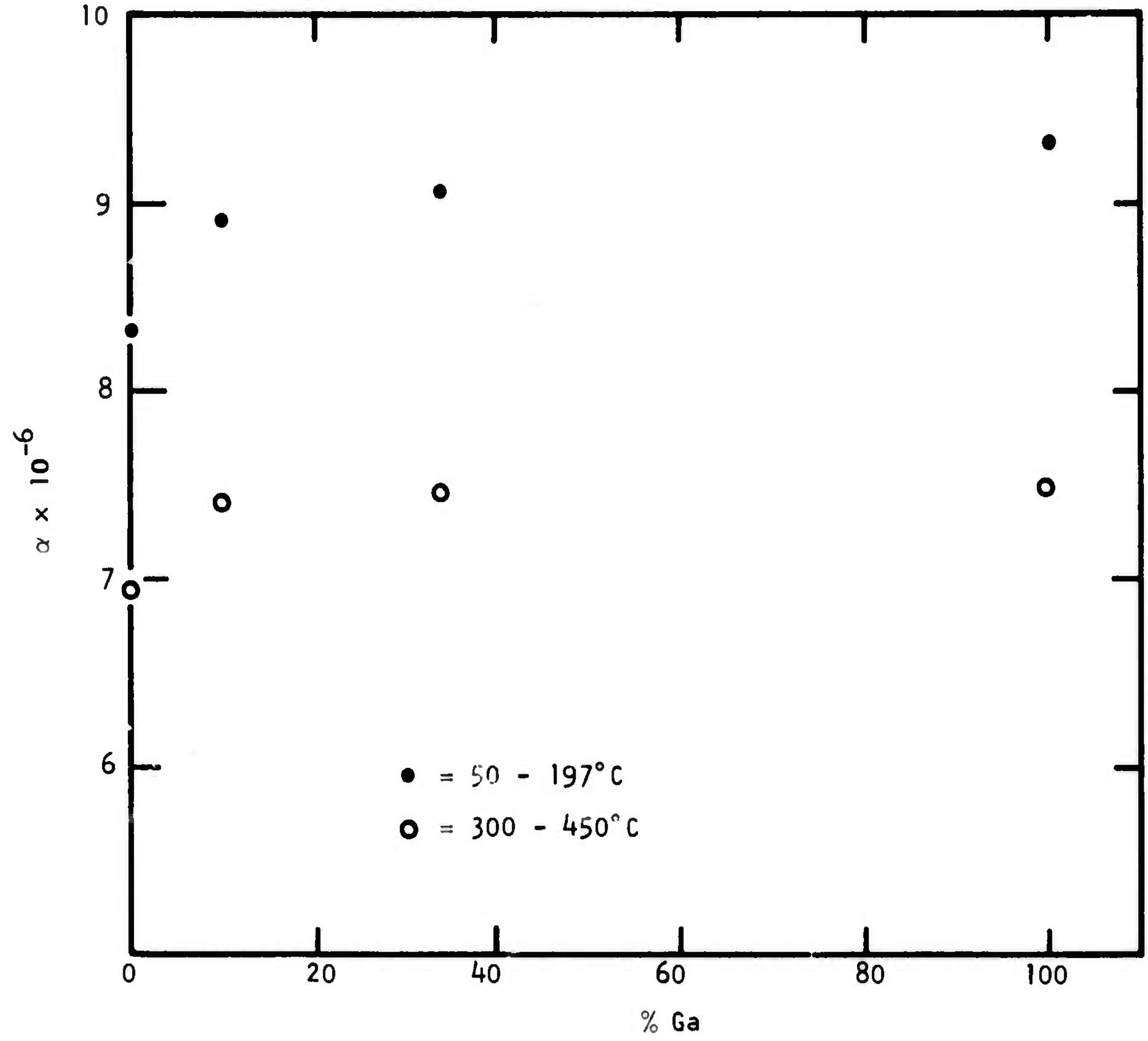

Figure 25 Thermal Expansion of YAGG

TABLE V

THERMAL EXPANSION OF YAGG

Sample	Temperature (°C)	α (°C^{-1})
YAG	50-147	6.95×10^{-6}
(0% Ga)	270-414	8.37×10^{-6}
YAGG #23	50-147	7.41×10^{-6}
(10% Ga)	367-485	8.91×10^{-6}
YAGG-I-6	74-197	7.45×10^{-6}
(34% Ga)	390-508	9.08×10^{-6}
YAGG-S-10	74-197	7.48×10^{-6}
(100% Ga)	319-461	9.33×10^{-6}

Microhardness measurements were made using a Riahle Kantron Microhardness Tester with a Knoop diamond indenter. Both 50 and 100 gram loads were tried. All indentations were made on (111) surfaces in areas midway between the core and the outside diameter of the crystals. No definitive values of hardness were obtained due to a combination of the hardness and brittleness of the samples. With the lighter, 50 gram load, the indentation was not sufficient to give any degree of accuracy to the measurement, and the scatter was considerable. Under a 100 gram load, most of the samples cracked, again reducing the accuracy. From a number of different samples tested, however, there appeared to be no serious degradation in the microhardness caused by the substitution of gallium in YAG.

Unit cell size was determined by x-ray precision lattice parameter measurements. The lattice parameter varies linearly with composition between the extremes of 12.005 Å for $YA\ell G$ to 12.227 Å for YGaG.

The refractive index vs wavelength was measured on three samples by the method of minimum deviation. Some traces of striations were seen in the mixed crystal prism. Wavelength accuracy is ± 30 Å, and the indexes are considered accurate to within ± 0.001. The results are given in Table VI. If we plot the index at 1.0867 μm vs composition and connect the end points $n(YA\ell G)$ and $n(YGaG)$ by a straight line, the point for $n(YA\ell_{0.9}Ga_{0.1}G)$ lies very near and slightly below the line.

The results of the physical measurements indicate that the most serious alterations in properties came with the initial introduction of small amounts of gallium, and that additional, larger amounts have a less pronounced effect. The properties apparently do not degrade to any degree that would seriously impair the mixed garnet as a good laser material.

TABLE VI

REFRACTIVE INDEX

λ (Å)	n(YAℓG)	n(YA$\ell_{0.9}$Ga$_{0.1}$G)	n(YGaG)
3962	1.860	1.872	1.987
4970	1.842	1.853	1.955
5954	1.832	1.842	1.940
6961	1.826	1.835	1.931
7980	1.822	1.830	1.924
8952	1.819	1.828	1.921
9876	1.817	1.825	1.918
10867	1.815	1.823	1.916

SECTION VI

LASER TESTING

A. Introduction

Laser tests were carried out to (1) establish an increase in the saturation level of the Q-switched output, and (2) evaluate the quality of the material obtained. The effect of fundamental physical quantities such as thermal diffusivity, temperature gradient of the index of refraction and thermally induced birefringence via the stress-optic effect all influence Q-switched laser performance and may determine the average power output. Manufactured quality of the material, such as optical path uniformity and inclusions, in turn, may limit the peak output energy available.

Because of extremely poor optical quality of the material, the evaluation of these laser parameters was unsuccessful for the six rods fabricated from three different boules of material. YAℓG:Nd begins to show saturation effects at 20 J input and an output of 100 mJ, and saturation is estimated at 150 mJ output at 40 J input. The best mixed crystal results show a threshold of 20 J and no saturation effects at an input of 80 J, but the output is still only 200 mJ. The low slope efficiency and high threshold result directly from poor optical quality.

The saturation effect is discussed only in relation to Q-switched laser operation, although it should be observable in the luminescences. The mechanism is that randomly directed photons are amplified by the gain medium and therefore reduce the population inversion. An increase in the pump level increases the gain, and this in turn causes a more severe reduction of the inversion. In addition, more photons at the laser transition are present from the pump source. The other sources of photons are spontaneous emission in the laser medium and amplified radiation returned by one of the laser resonator mirrors and the highly reflective pump cavity. The level at which saturation occurs may be raised by eliminating as much of this random radiation as possible. In practice, the laser rod is surrounded by an absorber at the laser wavelength.[13] The ends of the rod must be left clear, of course, so that two of the four sources of radiation that deplete the population inversion are left. The other way to increase the saturation level is to reduce the gain of the laser medium.

From this brief qualitative description of saturation it is clear that the quantitative results are dependent on the geometry of the pump cavity and the laser resonator and on the input level to the pump and hence threshold and slope efficiency of the laser material. The value of the saturated output is therefore only a relative quantity. Reports in the literature show it to be as low as 75 mJ for YAℓG:Nd,[14] although lasers with similarly sized YAℓG rods are run routinely at outputs of 26 mJ without showing saturation effects.[15] The level appears to be Q-switch dependent. Lasers with electro-optical Q-switches exhibit the saturation effects in the range of 100 to 200 mJ, but with acousto-optic Q-switches, outputs beyond 300 mJ have been obtained, at which point saturation may become obscured by a decrease in pump efficiency of the krypton flashlamp because of the spectral shift in its output at high drive levels.

Another effect that obscures measurement of the saturation level is inadequate stand-off by the Q-switch. Long pulse lasing action takes place even though the Q-switch is in the high loss state. The output is now a mixture of a Q-switched pulse preceded by the low-peak-intensity, but long-duration, long-pulse output. The effect is difficult to observe during operation, but it results in a linear input-output curve, since the energy measuring device responds to the total output. The presence of the effect is indicated by laser output at high input energies while the Q-switch is kept in a high loss state. The stand-off problem occurs with electro-optic Q-switches. It is dependent on their alignment and on the applied retardation voltage, both of which are adjusted for maximum stand-off. The stand-off for acousto-optic Q-switches is much higher and is not a problem. They suffer, instead, from a multiple output pulse at high energies. If saturation has not set in at this point, it cannot be measured with these Q-switches.

The optical quality of the laser material will determine the maximum power output of the laser. The factors separate into two classes: the fundamental physical constants of the material and the manufacturing defects.

The physical constants of importance are related to the thermal behavior of the laser rod. The ultimate power loading is determined by the rod fracture due to thermally induced stress. The magnitude of the temperature profile of the laser rod is determined by the thermal conductivity. The thermally induced focal length depends on the temperature gradient of the index of refraction and on the average stress - optic coefficient.[16] The anisotropy of the stress-optic components determines the thermally induced birefringence.[16] This quantity is difficult to correct for in the resonator and leads to poor beam divergence and poor performance with a conventional electro-optic Q-switch. A special design has to be used to retain both components of linear polarization in the resonator.[17]

The manufacturing defect that limits the average peak energy in the laser is inclusions. In the mixed crystal material the inclusion is iridium. The inclusion is a site at which fractures occur, growing in size until catastrophic damage occurs. Catastrophic damage was observed in one of the manufactured laser rods, and a number of small damage sites were also found in this and another rod from the same boule.

The existence of color centers in the material leads to solarization of the rod from the UV output from the flashlamp. Filtration of the light can eliminate this problem which was observed in the mixed crystal material.

Static optical quality is the final factor that determines laser performance. The evaluation is made from Twyman-Green interferometer fringe counts on the fabricated laser rods. Generaly, a dozen fringes can be seen for the two-inch long rods. The fringes are not straight and occasionally show abrupt shifts. Although this evaluation is subjective, it proved to be the overriding factor that prevented an evaluation of most of the laser-related parameters.

B. Simple Theory

The equations derived from simple theory are presented here. They are used later to plot the data and to pinpoint problems with the material.

The experimental results are obtained as an output energy vs input energy curve. Simple theory preducts this curve to be straight line.

$$E_o = (\tau_o/\tau_i)\ \sigma_s\ (E_i - E_t), \tag{20}$$

where E_o is the output energy, E_i the input energy, E_t the threshold input energy beyond which lasing occurs, τ_o the output pulse length, τ_i the input pulse length, and σ_s the slope efficiency. The formula is really derived in terms of power P, which is approximated as $P = E\tau$. The slope efficiency, in turn, is

$$\sigma_s = 2\eta\ (1 - R)/\ (1 + R)\ \ (L - \ell nR), \tag{21}$$

where R is the output mirror reflectivity, and L is the total roundtrip loss in the resonator excluding the output. The quantity η is an efficiency factor which converts the electrical input to the flashlamp into the pump rate into the upper laser level, viz.,

$$R_2\ (cm^{-3}\ sec^{-1}) = \eta\ P_i\ (watts)/h\nu(J)\ V(cm^3). \tag{22}$$

The energy of the absorbed photon $h\nu$ and the lasing volume V convert the rate R_2 into a power.

The threshold power is

$$E_t/\tau_i = A \cdot I_s \quad (L - \ell n\ R)/2\eta \quad , \tag{23}$$

where A is the cross-sectional area of the lasing volume. The saturation factor I_s is

$$I_s = h\upsilon_\ell/\sigma \cdot t_2 \qquad (\text{watts/cm}^2) \quad . \tag{24}$$

This formula contains the laser frequency υ_ℓ, the cross section σ, and the upper level spontaneous decay time t_2.

The quantity that can be changed in a series of measurements is R. Equation (23) thus provides a curve of E_t vs $(-\ell n\ R)$ from which the roundtrip loss L may be evaluated. The value of L and the measured values of σ_s can then be used to evaluate the efficiency η by use of Equation (21).

Evaluations of the parameters in these equations beyond this point become uncertain and do not generally show consistency. For example, (24) can be used to evaluate the cross section σ which does not generally correspond to the spectroscopic value. The loss factor L and efficiency η can be determined from the data $\sigma_s(R)$ and Equation (21). This value of L differs from that obtained from Equation (23).

These equations have been used with long-pulse laser results. Values of $L = 0.24$ to 0.80 have been found with the mixed crystal material. The value of η is about 0.01. The input-output curves are not linear, so that the assumptions underlying the equations are not well satisfied.

These equations show the following well-known properties of lasers. A high loss, L, causes a high threshold and a low slope efficiency, σ_s. A low conversion efficiency, η, has similar results. A low value of η may be caused by a low Nd concentration, a poor spectral match between flashlamp and Nd absorption, or poor optical transfer from lamp to rod. If only part of the rod shows laser action, then Equation (22) shows that η is small and the ratio η/V is constant. The result is that the threshold is not affected since A/η is constant. The slope efficiency is less than if the whole rod lases over its whole cross section.

Lasing action over part of the rod cross section has been encountered with the mixed crystal material. The cause is believed to be the severe optical path distortion indicated by the Twyman-Green interferometer.

C. Pump Cavity and Instrumentation

All the laser rods fabricated during this program were approximately 2 inches long. The pump cavity was therefore made 2 inches long. The cavity was elliptical with the major axis 0.825 inch and the minor axis 0.667 inch. The lamp and rod were placed on the major axis symmetrically with respect to the center and with a center-to-center spacing of 0.406 inch. This geometry had been determined previously to be optimum for 3 inch long YAℓG:Nd laser rods of 5 to 6 mm diameter. Flashlamps with 2 inch arc length and 3 mm bore diameter were used. Since an ellipse does not have unity optical magnification, better efficiency is obtained with a lamp bore of smaller size than the laser rod diameter. The cavity was polished and silver plated. Flat reflectors, also silver plated, were used at the ends. Cooling was done with distilled water flooding the whole pump cavity.

The flashlamps were standard ILC units filled to 1500 Torr with krypton. They were excited by a single mesh pulse-forming network with a time constant[18] of 55 μsec. This value was found to be an optimum for YAℓG:Nd. The power supply was capable of delivering 80 J into the flashlamp. Under these conditions, the maximum current limit into the flashlamp is exceeded by a factor of 2 to 4.

Lamp lifetime is very short, a few hundred to a thousand shots. Since third wire triggering becomes difficult and erratic after a few dozen shots, a series trigger was used.

The pulse energy was measured with an EEG radiometer model 580 with a narrow beam adaptor. The instrument is used in the current mode and is calibrated with a TRG model 100 ballistic thermopile. At pulse repetition rates below 5 per second, the radiometer does not provide sufficient damping, and the thermopile is used. Data were taken at 10 pps and at 1 pps.

D. Resonators and Q-Switches

For long-pulse operation a pair of flat mirrors was used with a resonator length of 8.5 inch. Repetition rates of 10 pps were used. Due to the static optical distortion of the mixed crystal rods the alignment of the resonator proved to be very difficult. The resonators were mounted on an Ealing lathe bed optical bench, and Lansing mirror mounts with differential screw adjustments were used. High quality laser mirrors from Perkin-Elmer were used.

The first two rods, fabricated from boule #23, were operated with an acousto-optic Q-switch. The resonator, shown in Figure 26(a), has an overall length of 28 inches. The Q-switch has a 6 mm active aperture and is driven with a 100 MHz, 2 µsec long pulse, from an Arenberg model PG 650 C. Two Porro prisms are used as the mirrors in this laser.

The other four rods were operated with an electro-optic Q-switch. The unit has a 3/8 inch diameter aperture, is made from KD*P, and has a window which retains the index matching fluid. A Glan air spaced polarizer is attached. An optimum resonator with the mixed crystal laser rods is formed with a high reflectivity 1.5 m radius mirror and a flat 35 to 40% reflectivity output mirror. Resonator length is 42 cm. Stand-off for this unit was fair. Long-pulse operation begins to appear at 40 J input to YAℓG:Nd when the switch is in the high loss state.

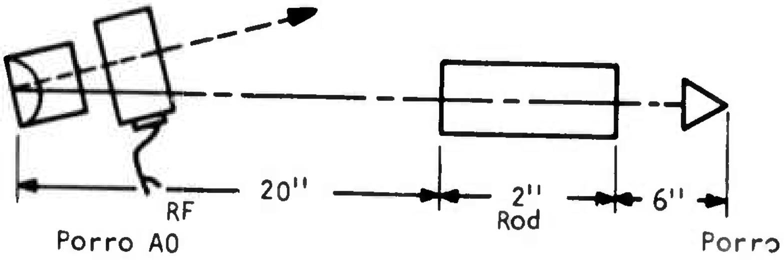

Figure 26(a) Acousto-Optic Q-Switch and Resonator

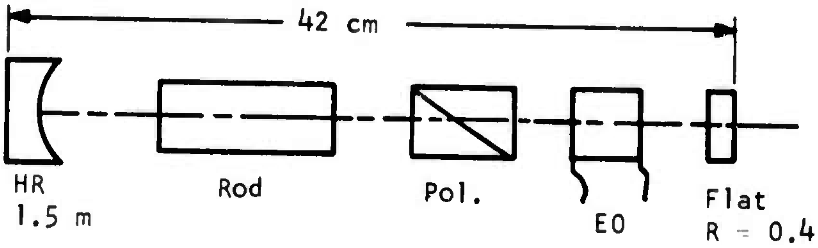

Figure 26(b) Electro-Optic Q-Switch and Resonator

The insertion loss of the Q-switch and polarizer combination is very low, estimated to be less than 3%.

E. YAℓG:Nd Operation

Input-output curves for Q-switched operation of YAℓG:Nd are presented in this section. The resonators are as described previously. The YAℓG rods were 1/4 inch in diameter and 2 3/8 to 3 inches long. Only the 2 inch length inside the flashlamp cavity is pumped. These results can then be compared with the mixed crystal runs described in the next section.

Figure 27 shows results at low input energies for long pulse operation. AO Q-switch operation and EO Q-switch operation were obtained with two flat mirrors and a 57 cm resonator length. Optimum mirror reflectivity for EO Q-switching is 0.3 to 0.4. The data show a Q-switched threshold of 3 J. Slope efficiency for AO operation is 1.75% and for EO operation it is 20%. These results were obtained at 10 pps.

Figure 28 shows the high input energy results with a resonator optimized for the mixed crystal rods. This resonator with EO Q-switch is described in the previous section, and data are taken at 1 pps to eliminate average thermal effects. The YAℓG rod is 5 mm in diameter. Slope efficiency is 1%, and threshold is extrapolated to be 5 J. The saturation limit is estimated to be 160 mJ. Although higher output energies are shown in the figure, they are a result of combined long pulse and Q-switched energies. This has been verified separately and can be deduced from the erratic behavior of the high output end of the curve. The smooth lower part of the curve is extrapolated to give the saturation value. Saturation effects are also apparent in Figure 27 at these output energies. The Q-switched curve begins to fall below the long pulse output. The saturation shown in Figure 28 may in part also be the result of spectral shifts in the flashlamp output.

In view of the mixed crystal results, no additional effort was spent on YAℓG laser behavior.

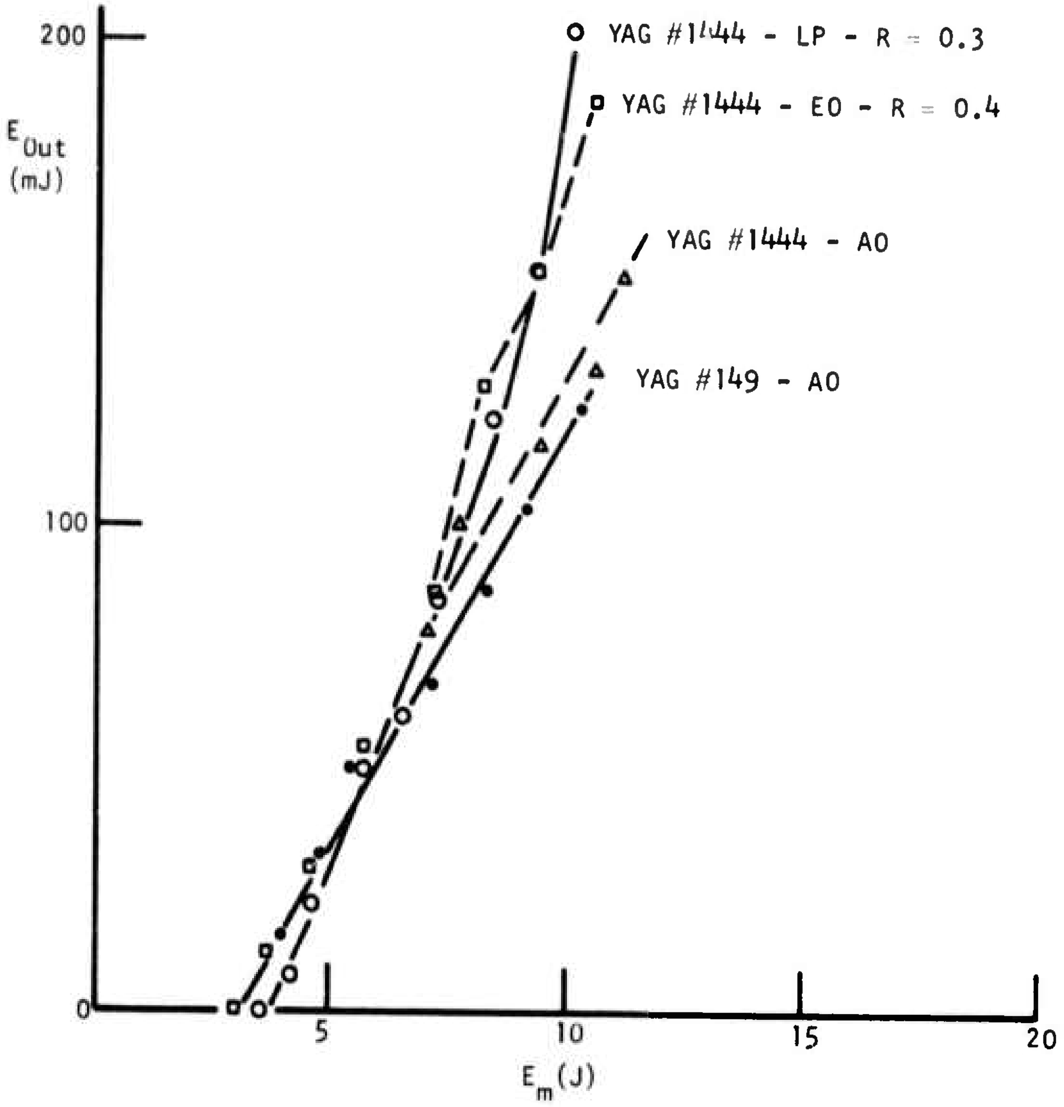

Figure 27 Long Pulse and Q-Switched Performance of YAℓG:Nd in Experimental Resonator

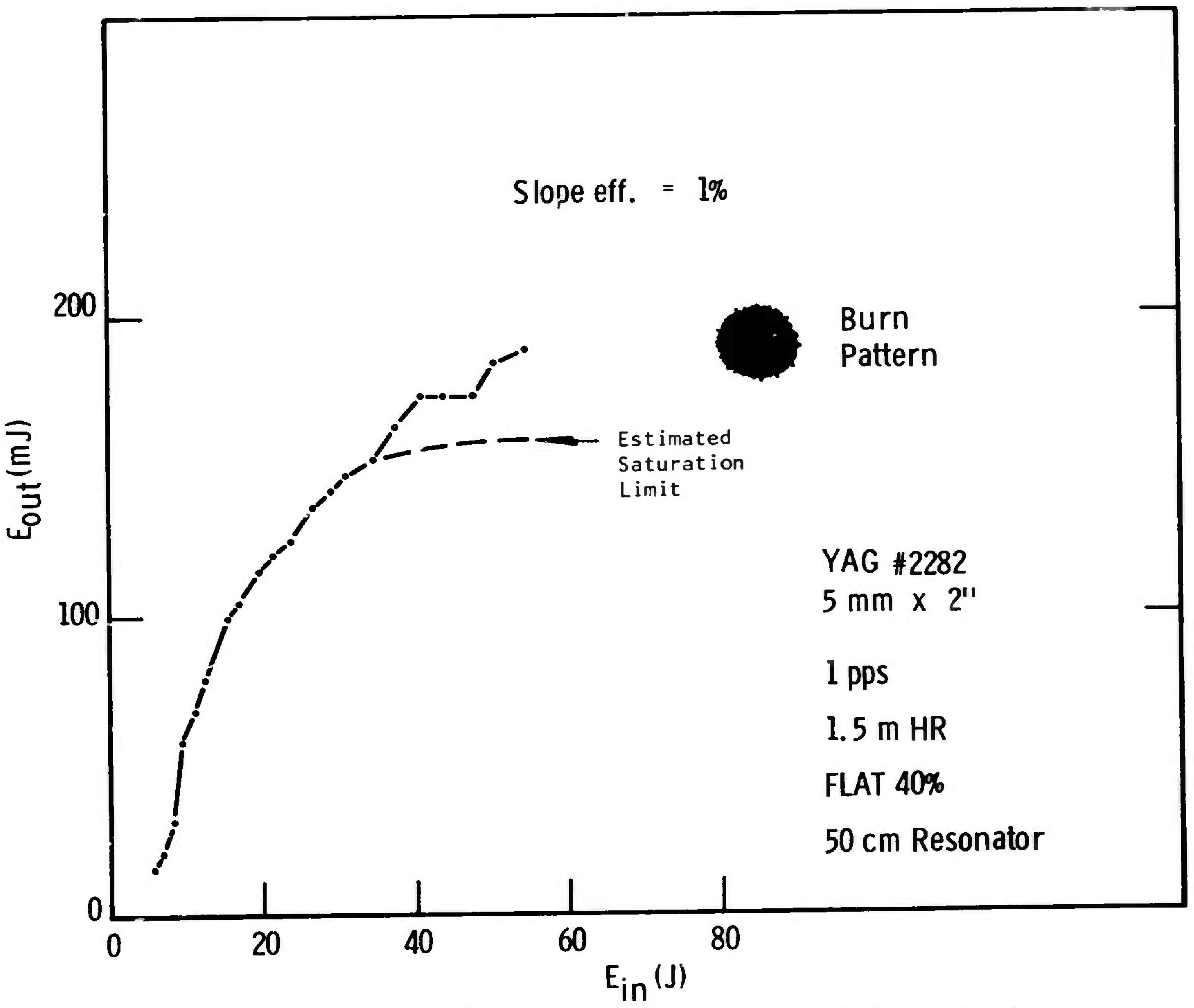

Figure 28 High Input Energy Q-Switched Performance of YAG

F. Twyman-Green Interferograms

Interferograms of the six laser rods fabricated are shown in Figure 29. The photographs were taken with He-Ne laser light. Two of the rods, 23-1 and 23-2, were fabricated to 6.3 mm diameter, the others to 5 mm diameter. All the rods are 2 inches long, except 47-A, which is 1.9 inches long.

The faces of the rods are flat to one or two fringes or better in the center. Generally, the surface quality of the AR-coated faces is not as good as that of commercially available YAℓG. A number of pits and coating blemishes can usually be seen. The rods also contain inclusions that can be seen with a microscope.

Figure 30 shows rod 23-1 positioned between crossed polarizers. The speckled radiation pattern is due to part of the boule core that was included in the side. Rod 23-2 is similar. The other rods were therefore fabricated to 5 mm diameter.

All the rods show a spherical to elliptical distortion with 5 to 10 fringes. In addition, 23-2, 45-6, and perhaps 45-B show abrupt path differences across the central aperture of the rod.

G. Nd Concentration

The concentration of Nd affects laser performance directly through the factor η in the equations.

The concentration in the top of boule 23 was compared with the concentration in a piece of a commercial YAℓG:Nd laser rod. The YAℓG contained nominally 0.9 at.% of Nd. The integrated absorption from 7760 to 8360 Å was compared. The ratio of the Nd concentrations is N(YAG)/N(YGG) = 1.5. The Nd concentration in subsequent boules was increased. A comparison between material from boule 42 and a commercially obtained boule showed N(YAG)/N(YGG) = 1.04.

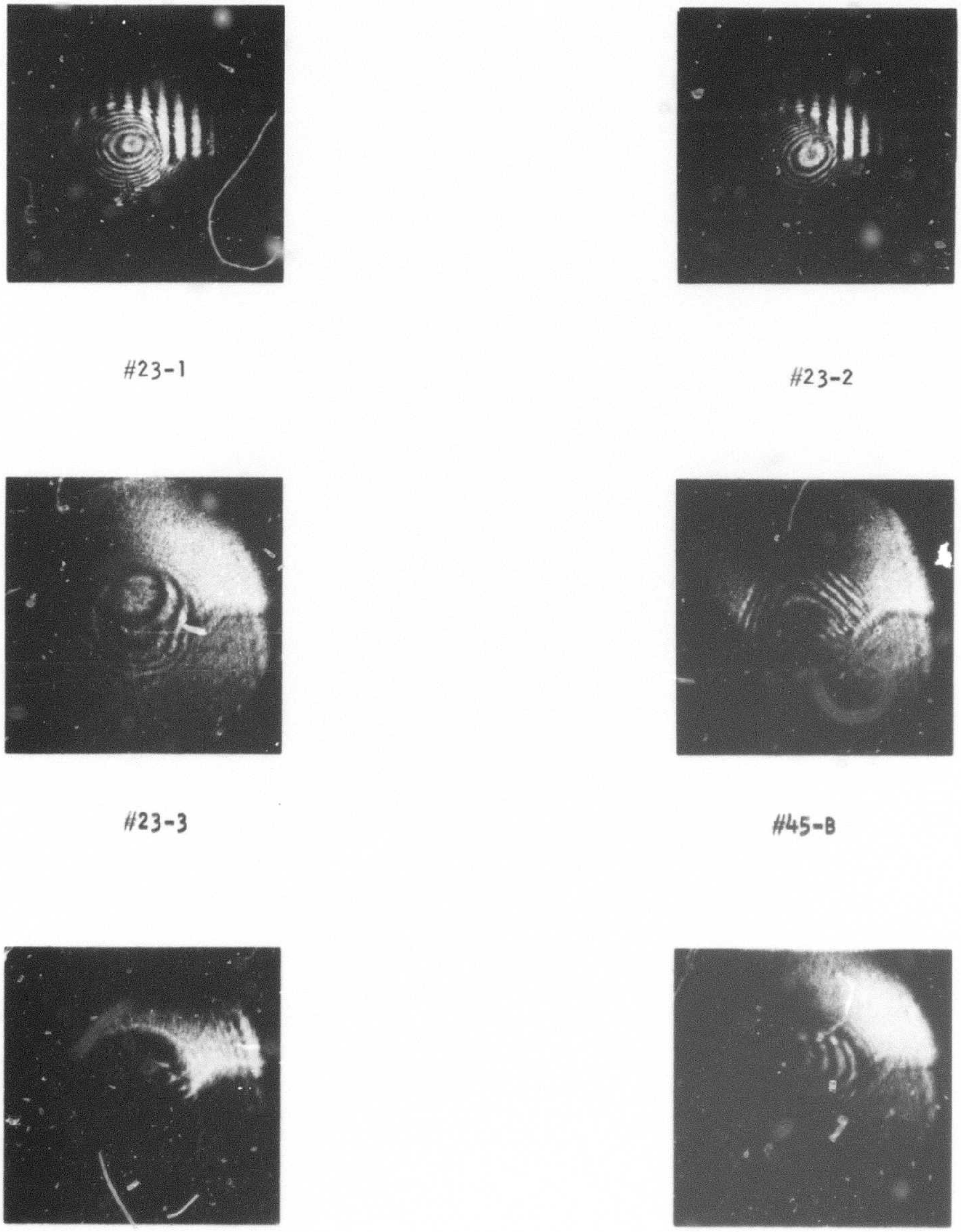

#23-1

#23-2

#23-3

#45-B

#45-C

#47-A

Figure 29 Interferograms of the Six Mixed Crystal Laser Rods

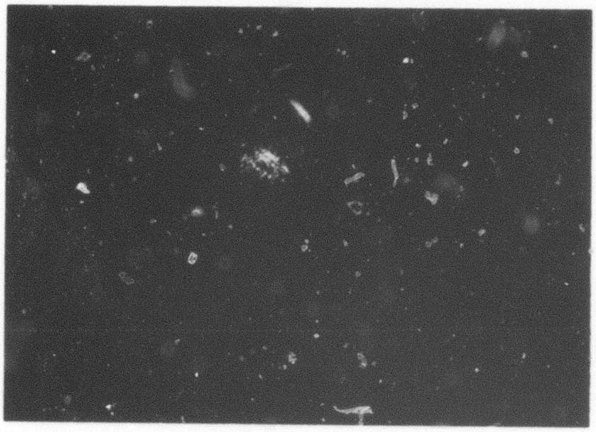

Figure 50 #23-1 Viewed through Crossed Polaroids

H. Long-Pulse Measurements

Long-pulse input-output curves were obtained with rod 23-1 in order to estimate the losses. Typical data are shown in Figure 31.

A plot of mirror reflectivity vs threshold energy is shown in Figure 32. Extrapolation of this curve indicates a roundtrip loss of 80%. Such a large loss term, along with the lack of straight lines in Figures 30 and 31, shows that the approximations in the laser equations are not well satisfied. This is borne out by the lack of self consistency of the data. Figure 33 shows a plot of $\sigma_s/2\eta$ vs R. An optimum fit is obtained for $\eta = 1\%$ and $L = 24\%$ using Equation (21). L is varied and η is calculated for each measured slope efficiency. The best fit is that value for L for which the standard deviation of the calculated η values is a minimum. If the loss factor L is taken to be 80%, a value of η of 2% is calculated.

The cross section σ may be calculated from Equation (24). The value of I_s is obtained from Equation (23). It is the slope of the curve in Figure 32. The value of σ obtained this way is 2 to 5×10^{-19} cm^2.

Although quantitatively not very satisfactory, these tests show the results of the poor optical quality of the material as exhibited by the Twyman-Green interferograms. During tests, the rod showed a general darkening, i.e., a solarization. No further long pulse data were taken so as to avoid this deterioration before Q-switching was tried. The darkening can be annealed out of the material in 15 minutes at 360°C.

I. Q-Switched Measurements

Rods 23-1 and 23-2 were operated in the acousto-optic resonator. The results are shown in Figure 34. A comparison curve for YAℓG:Nd is included.

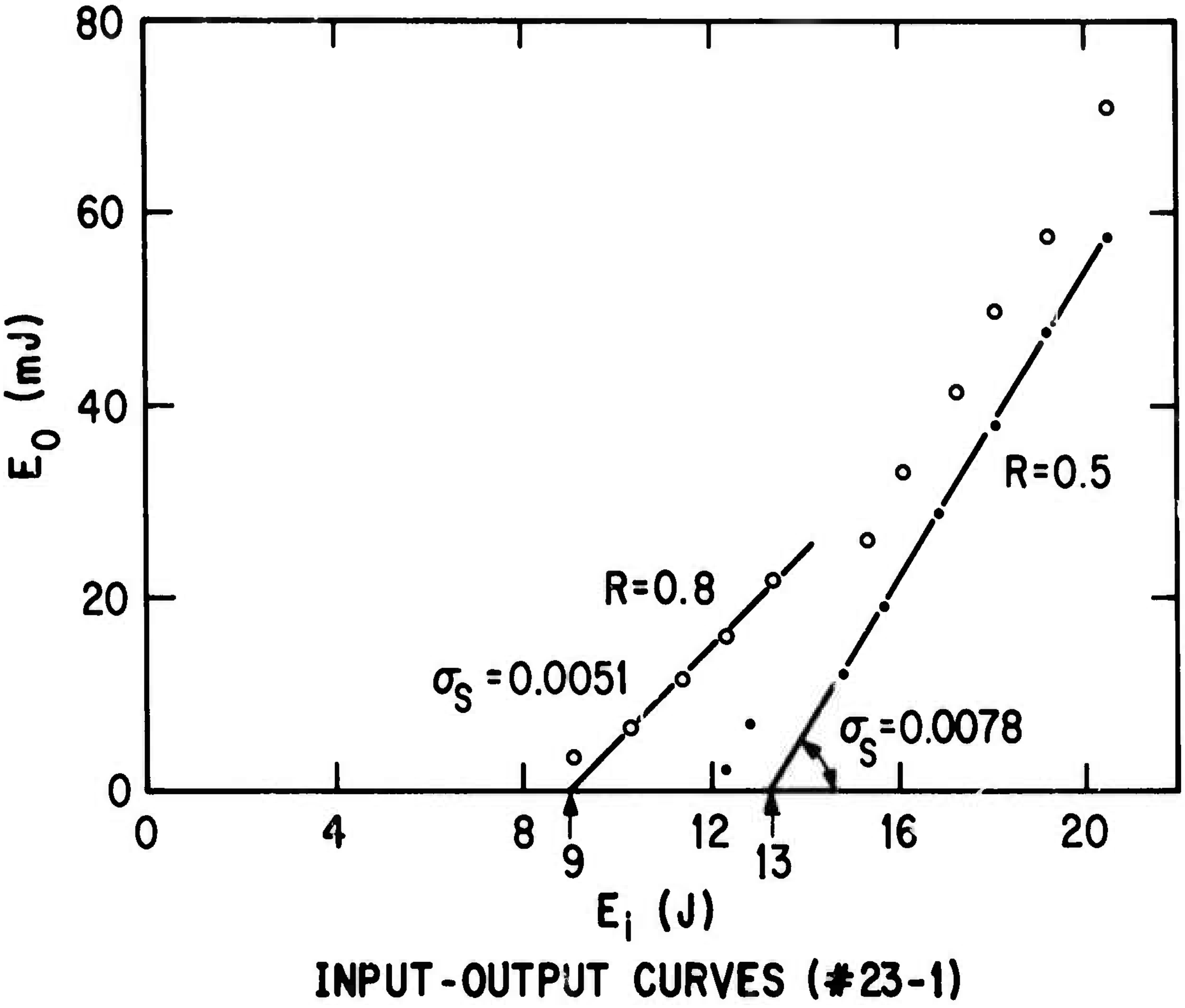

Figure 31 Input-Output Curves Under Long Pulse Conditions. Resonator length is 8.5 inches. The mirror reflectivity R is varied, and threshold, E_t, and slope efficiency σ_s, are determined from the data.

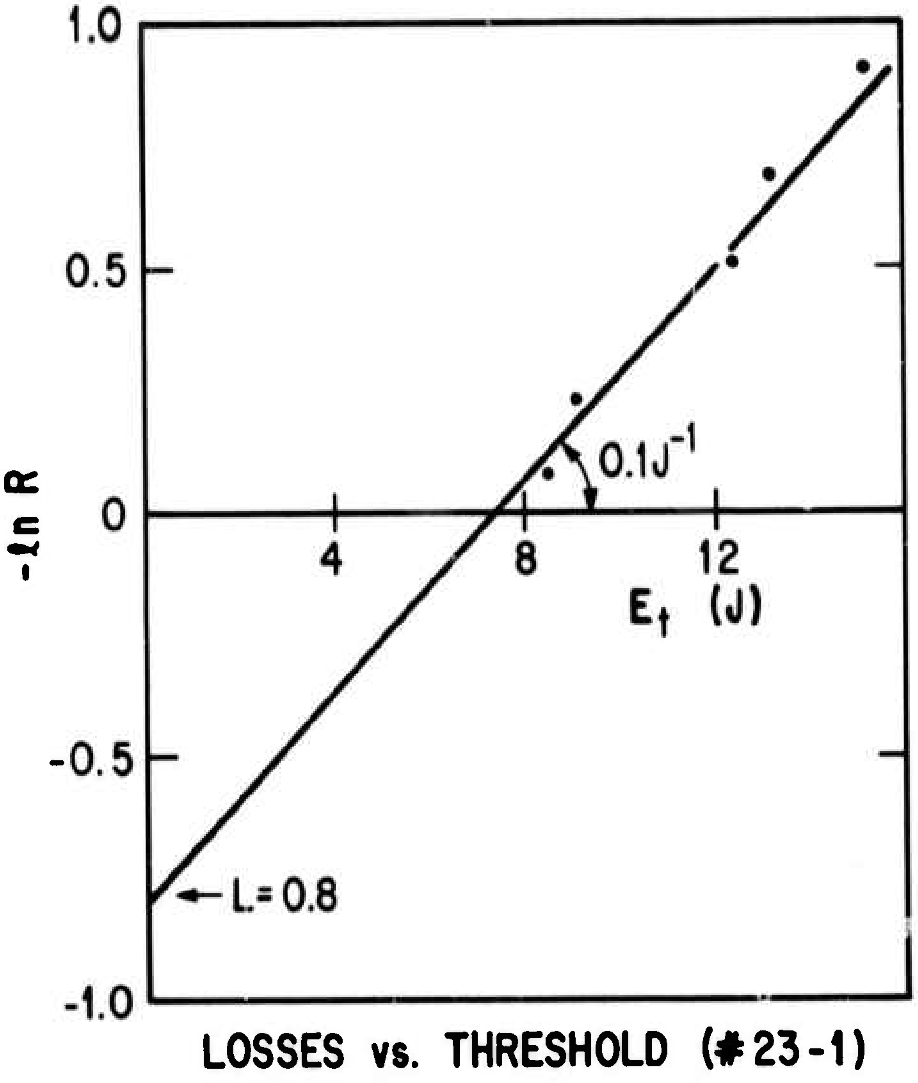

Figure 32 Known Mirror Losses vs the Observed Threshold Energies. A straight-line fit to the points extrapolates to a loss of 80%.

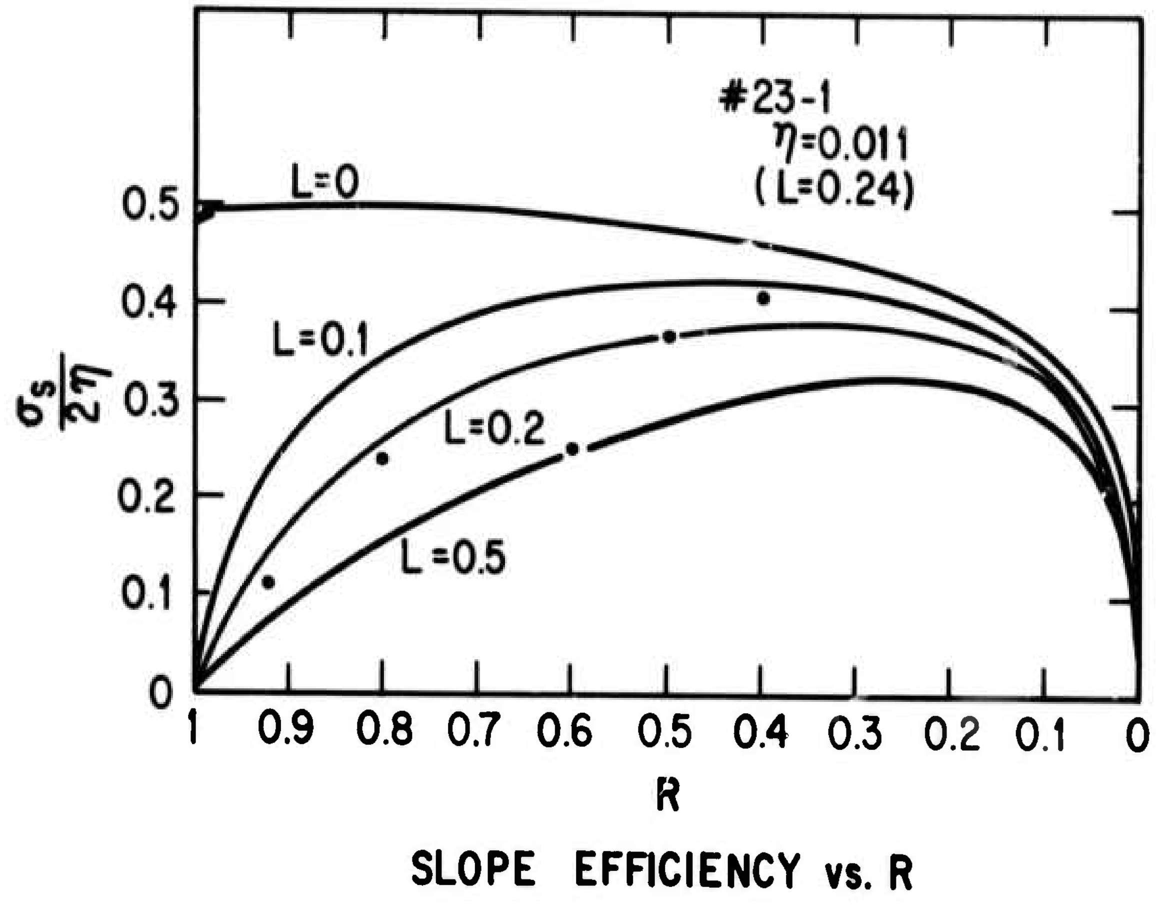

Figure 33 Calculated Values (Solid Lines) of $\sigma_s/2\eta$ vs R for Various Values of Loss L. The data points are plotted for the best fit η = 0.011 and L = 0.24.

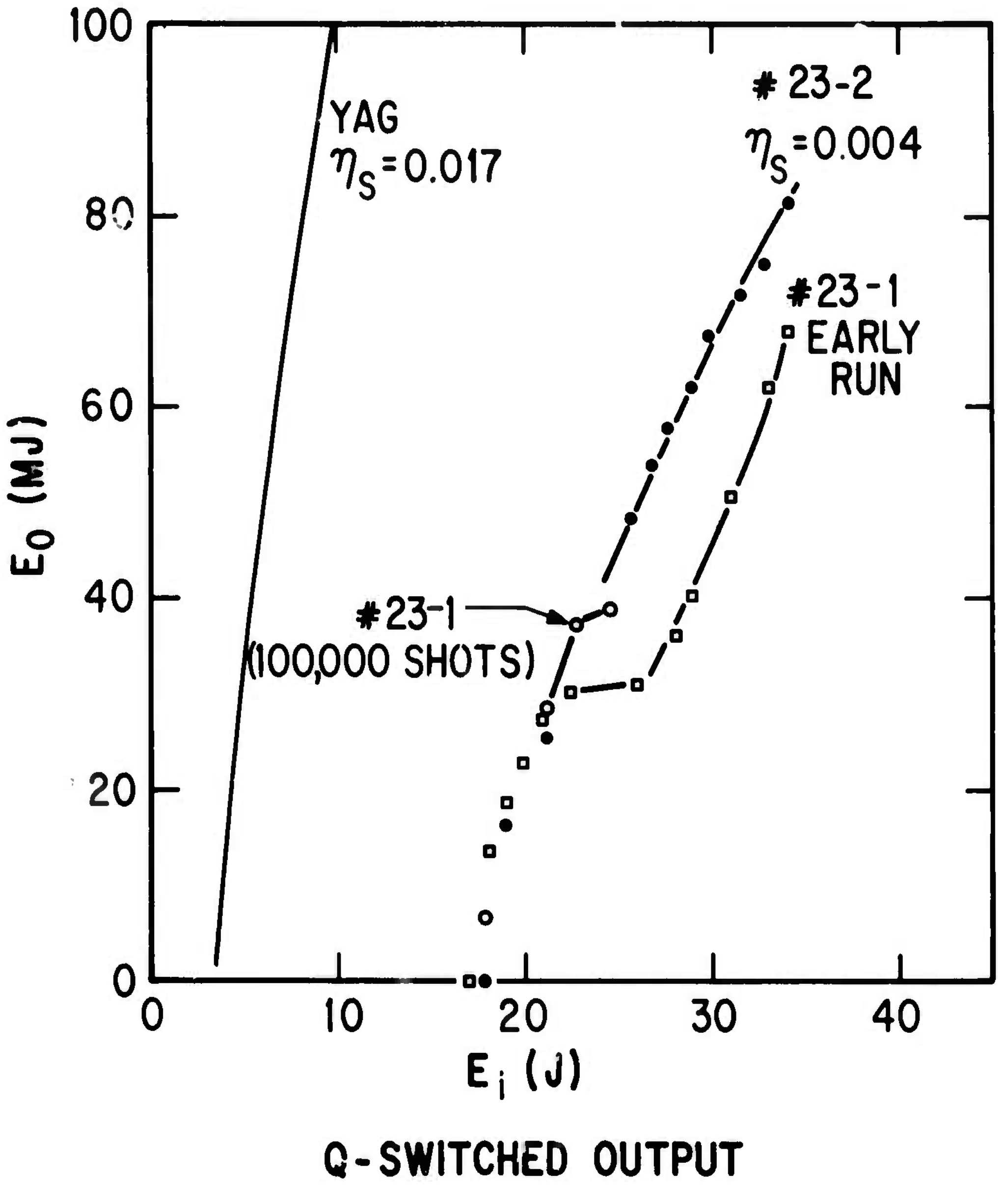

Figure 34 Input-Output Curves of YAG and YAGG:Nd. The slope efficiency η_S is shown for the two materials. For YAGG the curves are terminated where post-pulsing occurs. After 100,000 Q-switched pulses, this post-pulsing limits the output to half the original one.

The curves show the expected behavior: high threshold and low slope efficiency. This is because of the high optical losses and the low Nd concentration. The data are taken at 10 pps. Rod 23-1 shows what appears to be thermally induced distortion and consequent increased losses at 22 J input. Beyond 34 J input the rods begin to post-pulse and no meaningful data can be extracted beyond this point with the AO Q-switch. From the trend of the curves, no significant saturation effects would have been observable at 80 J input, the power supply limit. After 100,000 shots, post-pulsing set in at 25 J input. Threshold was 17 to 18 J, compared to 3 J for YAℓG. Slope efficiency was 0.4%, compared to 1.7% for YAℓG.

The next rods were run with an electro-optic Q-switch to avoid the post-pulsing problem. During the initial stages of EO Q-switching a 60 cm resonator with two flat mirrors was used. Very poor results were obtained with rod 45-B. The resonator was therefore changed to increase the output. The problem with rod 45-B was that lasing action tended to be confined to a central strip of the cross section of the rod, which results in a low slope efficiency. Long pulse data are shown in Figure 35. The area that takes part in the laser action changes with input power, so the results are difficult to interpret. The resonator was therefore changed to its final configuration. During the course of these changes, the rod sustained optical damage. Near one end a large "bubble" appeared, and a number of smaller damage centers are visible near the center of the rod. Damage appears to nucleate at inclusions deposited along the growth interface of the boule. During resonator optimization, outputs of 131 mJ at 50 J input and 96 mJ out at 38 J input were obtained.

Rod 23-3 was run next. Data were taken with the resonator configuration described in Section VI.D at 1 pps. The results are presented in Figure 36. Best results were obtained with a 40 J PFN. Saturation appears to limit the output to 210 mJ. The entire cross section of the rod yields output during the Q-switching. Threshold was 10.7 J, and initial slope efficiency was 1%.

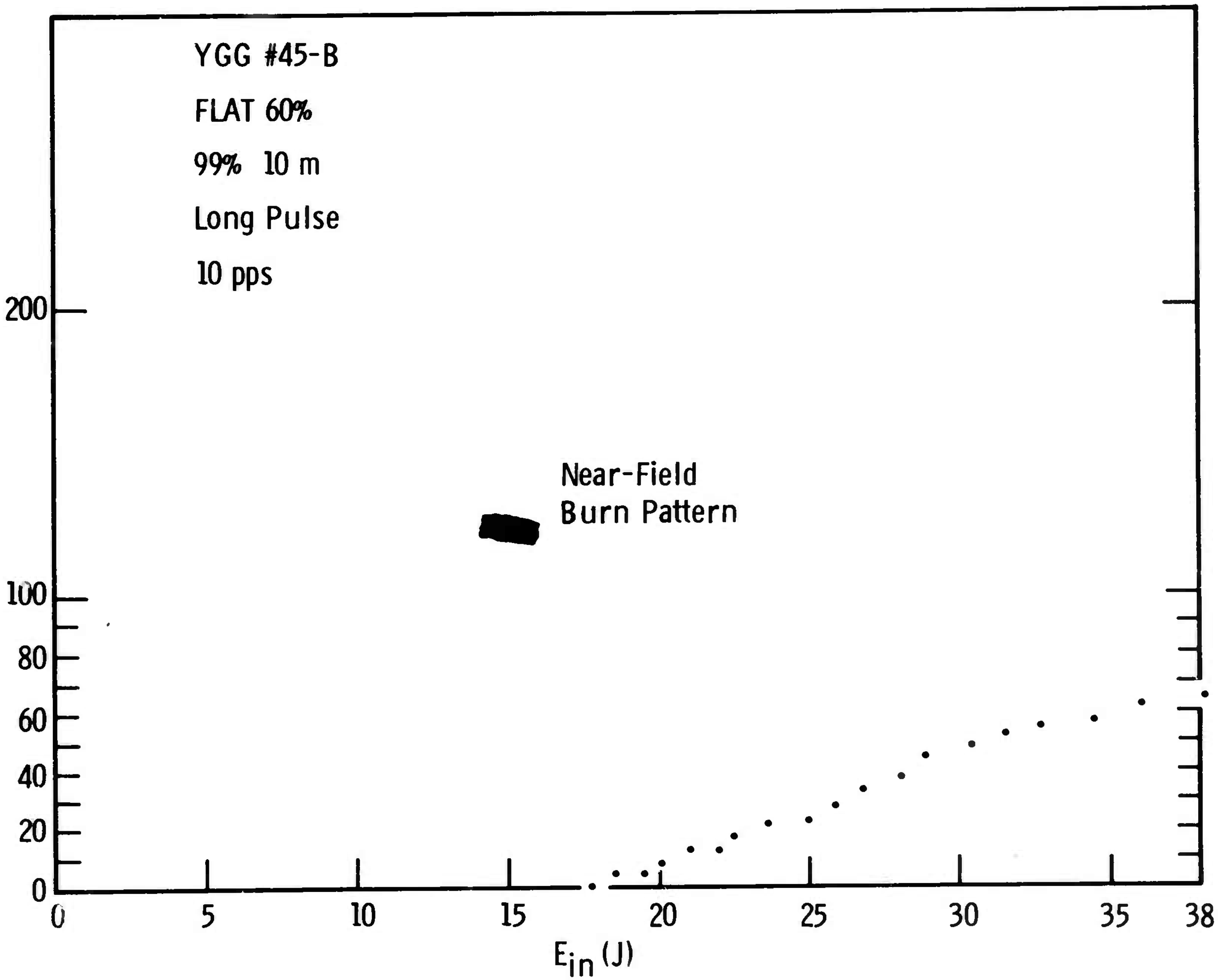

Figure 35 Long-Pulse Operation of 45-B Before Rod Damage Occurred

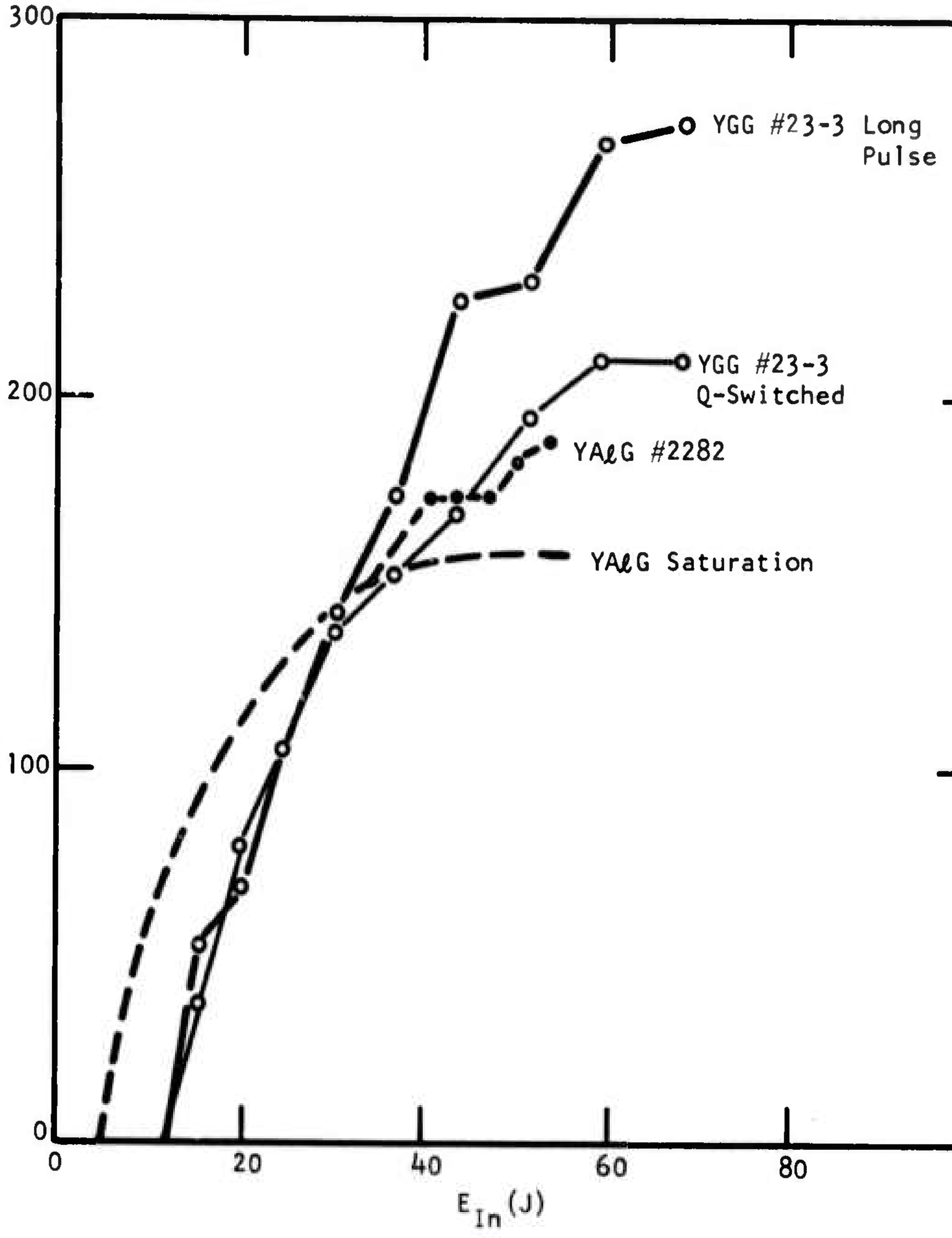

Figure 36 Saturation in Rod 23-3

Since this boule contains only a 10% Ga admixture, only a moderate increase in saturation is expected.

Rod 47-A was run next. The results are shown in Figure 37. Operation was very poor. Again, only a small part of the rod was active in the Q-switch process. No useful data could be extracted.

Finally, rod 45-C was run. To avoid the solarization process, the rod was surrounded by a nonex glass tube to filter out the ultraviolet. The results are presented in Figure 38. No saturation effects are seen at 80 J PFN. The voltage limit of the power supply is reached here with the 3 mm x 2 inch lamp and the 55 μsec PFN time constant. Threshold is 18.3 J. Slope efficiency is 0.5%. Again, only part of cross section of the rod is active during Q-switched operation. Near-field burn patterns at 170 mJ output are shown in Figure 39.

At the conclusion of the tests, some internal damage is visible in the rod. It seems similar to that in rod 45-B and appears at small inclusions near the middle of the rod. To avoid the damage as much as possible, only 100 to 200 shots were fired with rod 45-C. All data were taken at 1 pps.

J. Conclusions

A slight increase in saturation has been observed with a 10% Ga admixture.

Saturation could not be reached with the 40% Ga admixture material due to poor optical quality. The low slope efficiency would require inputs to the flashlamp of the order of 160 J to reach the expected saturation level.

The poor optical quality is evidenced first as a high lasing threshold. Its second manifestation is that only part of the cross section of the rod is active during lasing. This reduces the slope efficiency.

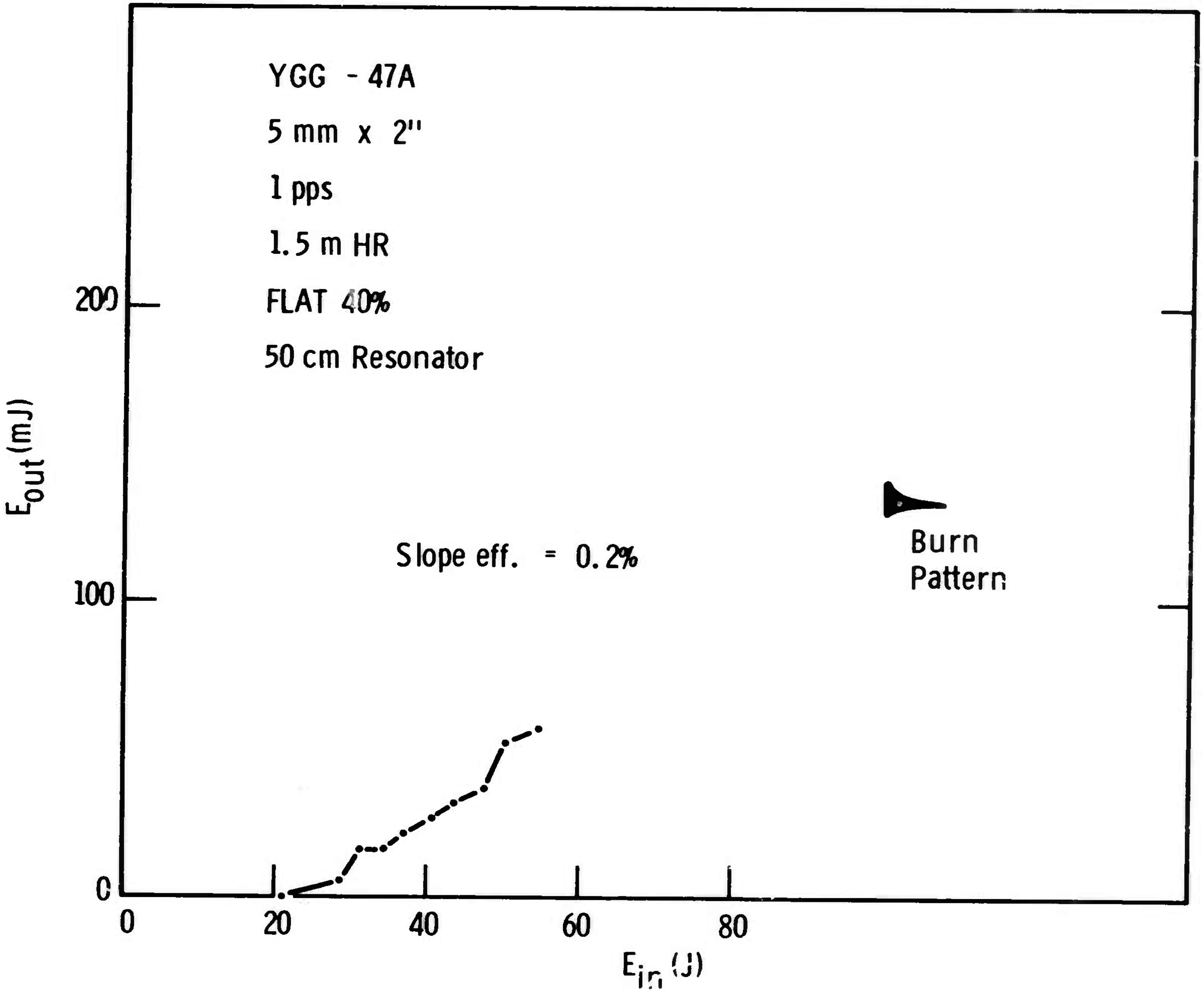

Figure 37 Rod 47-A Q-Switched Operation

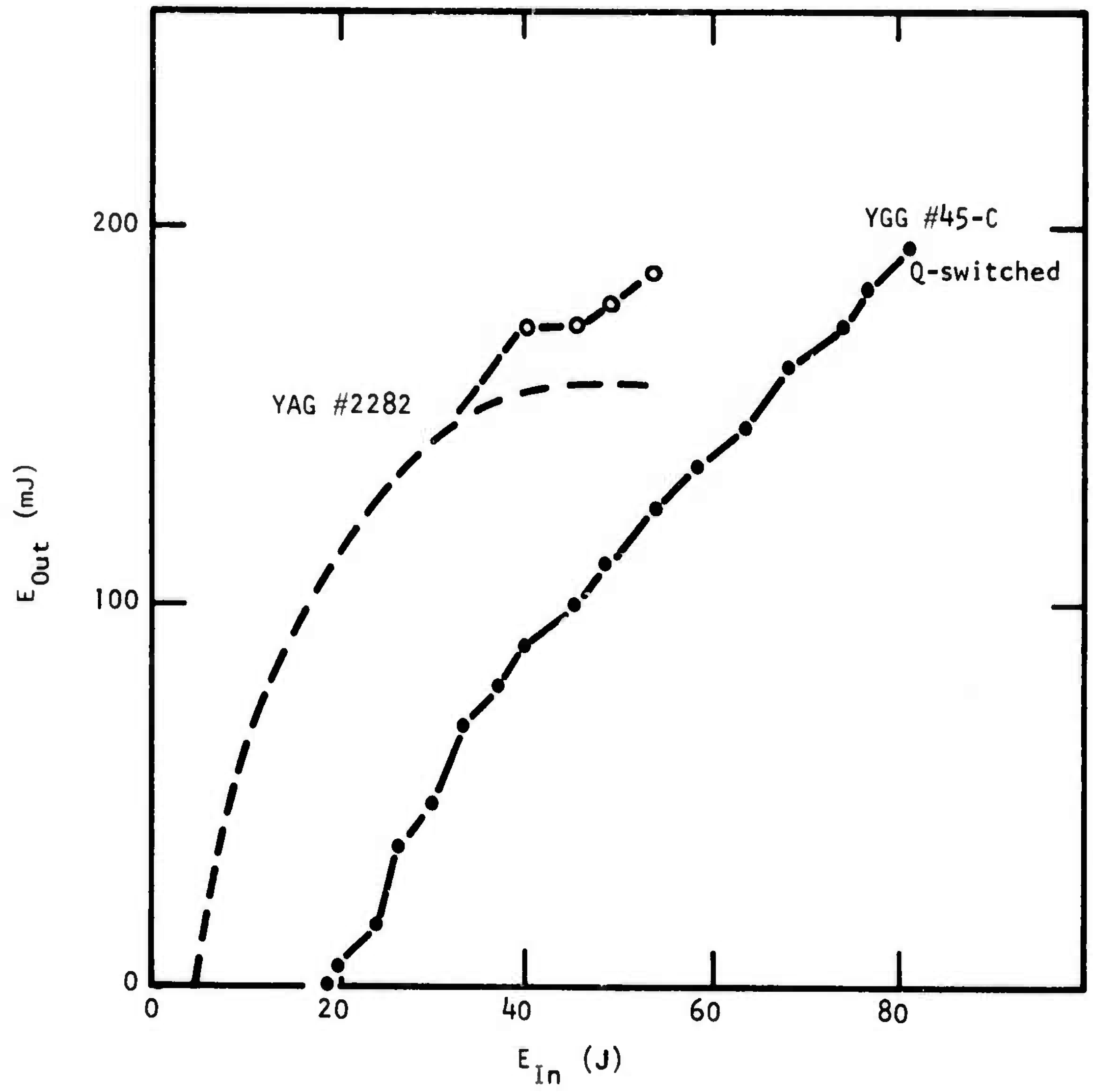

Figure 38 Rod 45-C Q-Switched Operation

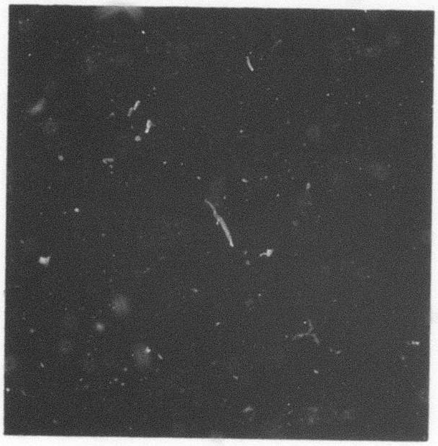

Figure 39 Near Field Burn Patterns at 170 mJ for Rod 45-C

Inclusions result in optical damage to the rods at output energies of 150 to 200 mJ. Energy densities are difficult to estimate at this time.

Color centers that lead to solarization are present. Solarization may be prevented by appropriate UV filtering.[19]

SECTION VII

SUMMARY AND CONCLUSIONS

Optical spectroscopic measurement showed that a decrease in peak cross section of the laser line by a factor of three with respect to YAℓG:Nd is possible in the YAℓG-YGaG mixed crystal system. A greater decrease would have been possible had the details of the dependence of Nd^{3+} energy level positions on composition been different. Thus, there may be other mixed crystal systems in which a larger decrease could be realized. The minimum in peak cross section as a function of composition is shallow, any composition near mid-range (40% to 70% Ga) being satisfactory.

The Nd^{3+} ion site distribution in the mixed crystal system was studied, and two types of Nd-Ga clustering were determined by electron paramagnetic resonance spectroscopy. The effect of inhomogeneous broadening on spectral diffusion of excitation across the line was determined. The lifetime of the $^4F_{3/2}$ initial state was found to vary only within narrow limits as a function of Ga content and to depend on Nd concentration in much the same fashion as in YAℓG.

Distribution coefficients for Nd and Ga in the mixed crystal were determined, and system phase diagrams were established. Thermal conductivity was found to decrease with increasing Ga content, the decrease being 35% (with respect to YAℓG) at 40% Ga. Thermal expansion, unit cell size, microhardness, and refractive index were also determined as a function of composition.

Six laser rods from three mixed crystal boules were tested under Q-switched conditions. Because of the poor optical quality of the material no definitive comparison of intrinsic characteristics could be made with those of YAℓG. The low slope efficiency and high thresholds observed with the mixed crystal rods result directly from the poor optical quality. Iridium inclusions were observed to act as nucleation centers for optical damage. Twyman-Green interferograms reveal severe distortions in optical path through the material. The distortions arise from strain that may be associated with the core of the boule or that may be due in part to compositional inhomogeneities. Solarization of the rods by the pump lamp was also observed. Six rods (2 inches long, 1/4 inch in diameter) were delivered.

In conclusion, although the mixed crystal material has potential advantages, it is not possible to realize this potential because of the difficulty of growing crystals of high optical quality. The difficulty is due to the volatility of gallia at the high growth temperatures and the sensitivity of composition to temperature fluctuations. While these problems might eventually be ameliorated somewhat in a research program of longer duration, it is possible that they could be circumvented entirely by choice of another mixed crystal system.

REFERENCES

1. M. M. Mann and L. G. DeShazer, J. Appl. Phys. 41, 2951 (1970).
2. M. J. Weber, M. Bass, R. R. Monchamp, and E. Comperchio, "Czochralski Grown Laser Materials," Technical Report AFML-TR-70-258 (December 1970).
3. P. Mauer, Appl. Optics 3, 433 (1964).
4. M. J. Weber and T. E. Varitimos, to be published.
5. J. A. Koningstein, J. Chem. Phys. 44, 3957 (1966).
6. T. Kushida, H. M. Marcos, and J. E. Geusic, Phys. Rev. 167, 289 (1968).
7. R. K. Watts, J. Opt. Soc. Am. 61, 123 (1971).
8. L. G. DeShazer and L. G. Komai, J. Opt. Soc. Am. 55, 940 (1965).
9. M. T. Hutchings and W. P. Wolf, J. Chem. Phys. 41, 617 (1964).
10. W. P. Wolf, M. Ball, M. T. Hutchings, M. J. M. Leask, and A. F. G. Wyatt, J. Phys. Soc. Japan Suppl. 17, 443 (1962).
11. M. Marezio, J. P. Remeika, and P. D. Dernier, Acta Cryst. B24, 1670 (1968).
12. J. D. Foster and L. M. Osterink, Appl. Optics 7, 2428 (1968).
13. T. G. Crow and T. J. Snyder, "Techniques for Achieving High Power Q-switched Operation in YAG:Nd," Technical Report AFAL-TR-70-69 (May 1970).
14. M. Bass and M. J. Weber, Appl. Phys. Letters 17, 395 (1970).
15. R. F. Hotz, M. deWit, and W. C. Scott, Texas Instruments Technical Reports, 1972.
16. J. D. Foster and L. M. Osterink, J. Appl. Phys. 41, 3656 (1970).
17. e.g., a birefringent prism to separate the two linear polarization components.
18. J. P. Markiewicz and J. L. Emmett, IEEE J. Quantum Electronics QE-2, 707 (1966).
19. Private Communication From V. Donlan, Air Force Materials Laboratory, Wright-Patterson Air Force Base, Ohio.